

1 **Validation of Rainfall Data Observed by Using Disdrometer under**  
2 **Wet-Bulb Temperature Conditions**~~Assessment of Disdrometer Data~~  
3 ~~Quality Control Methods for Precipitation Measurements Based on~~  
4 **Wet-Bulb Temperature**

5 Hyeon-Joon Kim<sup>1</sup>, Sung-Ho Suh<sup>2</sup>, Jongyun Byun<sup>3</sup>, Changhyun Jun<sup>4</sup>

6 <sup>1</sup>Center of Oceanic and Meteorological Information, Pukyong National University, Busan, South Korea

7 <sup>2</sup>Flight Safety Technology Division, NARO Space Center, Korea Aerospace Research Institute, Goheung, South Korea

8 <sup>3</sup>Department of Civil, Environmental and Architectural Engineering, Korea University, Seoul, South Korea

9 <sup>4</sup>School of Civil, Environmental and Architectural Engineering, Korea University, Seoul, South Korea

10  
11 *Correspondence to:* Changhyun Jun (cjun@korea.ac.kr)

12 **Abstract.** This study focuses on the reliability assessment of precipitation data calculated from drop size distribution (DSD)  
13 based on disdrometer data observations according to wet-bulb temperature ( $T_w$ ). Three distinct quality control (QC) methods  
14 based on fall velocity were implemented and validated against measurements from tipping-buckets and weighing rain gauges  
15 collected from January 2020 to February 2024. The analysis indicated that all QC methods exhibited high reliability  
16 (correlation coefficient (CC) > 0.98) for rainfall conditions when  $T_w$  was above 5 °C, with a mean absolute percentage error  
17 (MAPE) of approximately 8.5%. However, the precision of precipitation measurements exhibited a notable decline when  $T_w$   
18 was below 2 °C, as indicated by a CC of less than 0.6 and MAPE exceeding 30%. This reduction in accuracy can primarily  
19 be attributed to the outcomes of the QC methods, which rely on the falling velocity, given that raindrops and solid particles  
20 were observed within the specified  $T_w$  range. When considering the melting of snow particles at  $T_w$  ranging from 0 °C to 2 °C,  
21 the CC approached 0.9, suggesting enhanced measurement reliability. The findings of this study indicate that  $T_w$  is a more  
22 effective variable than air temperature ( $T_{air}$ ) for differentiating the precipitation types. This conclusion arises from the  
23 observation that the fall velocity of hydrometeors does not reach the terminal velocity of raindrops, even within the  $T_{air}$  range  
24 of 1–5 °C, coupled with the broad distribution of fall velocities. The DSD shape demonstrated stability across multiple QC  
25 methods when  $T_w$  was equal to or greater than 2 °C. In contrast, considerable variations were observed at lower temperatures,  
26 where particles with diameters ranging from 1 to 2 mm exhibited irregular distribution patterns at temperatures below 1 °C.  
27 These results suggest that DSD parameters should be derived from disdrometer data obtained under conditions where  $T_w$  is  
28 above 2 °C to ensure the reliability of the findings. This study provides critical insights for improving precipitation  
29 measurement techniques and DSD analyses in regions with variable temperature conditions.

## 30 **1 Introduction**

31 Several factors influence the variability in precipitation development, including atmospheric water vapor content, vertical  
32 airflow intensity, and temperature and humidity distributions in the vertical profile (Lintner et al., 2017; Padullés et al.,  
33 2022). These factors can be categorized as climatological, geographical, or topographical. Climatological factors include  
34 alterations in atmospheric water vapor resulting from long-term temperature changes, developmental shifts associated with  
35 temperature variations in the upper and lower atmospheric layers, and thermodynamic effects linked to changes in land cover  
36 based on climatic characteristics (Dahlström, 2021; Lu et al., 2024). Geographical and topographical factors include the  
37 convergence of water vapor due to mountainous terrain, which facilitates vertical precipitation development (Insel et al.,  
38 2010; Lee et al., 2014; Kim et al., 2019), and the generation of vertical flow resulting from increased friction at low levels  
39 due to coastal topography (Du and Chen, 2019; Yao et al., 2021). Additionally, precipitation development can be influenced  
40 by the temperature differential between the sea and air, particularly when cold air from inland regions moves over water  
41 bodies during winter (Steenhurg, 2020). Various environmental factors can influence the disparities in warm precipitation  
42 processes, such as collision-coalescence, evaporation, and accretion, which are contingent upon the vertical development of  
43 precipitation types, including stratiform, convective, and typhoon-related precipitation. Similarly, cold precipitation  
44 processes such as snow riming, melting, and ice crystal growth are affected by these environmental variables. These factors  
45 contribute to the development of diverse hydrometeors including rain, snow, and graupel, which are influenced by  
46 temperature variations (Maheskumar et al., 2018; Yi et al., 2021). The differences in the precipitation development processes  
47 ultimately lead to variations in the total precipitation observed at the surface. Therefore, it is crucial to acquire data that  
48 accurately reflects the microphysical characteristics of precipitation to enhance precipitation monitoring. Furthermore,  
49 analyses based on long-term observational data are essential to identify the universal characteristics that account for the  
50 temporal variability of precipitation.

51 The utilization of long-term observational data considerably reduces errors, mainly by rectifying inaccuracies in the  
52 observational data and eliminating outliers. Even among instruments that measure the same meteorological parameters, the  
53 threshold values for outlier removal may vary based on the installation conditions and surrounding environment.  
54 Additionally, biases in the observed values can arise owing to variations in the observation area and resolution, which are  
55 contingent on the type of instrument employed (Sypka, 2019; Segovia-Cardozo et al., 2021). Ground-based rain gauges can  
56 be categorized into two types based on their measurement method: tipping-buckets and weighing gauges. Although the  
57 tipping-bucket type demonstrates high accuracy in measuring rainfall, its efficacy in measuring snowfall during winter may  
58 be inferior to that of the weighing type because the observation value is recorded only when the precipitation in the bucket  
59 reaches a predetermined capacity (Savina et al., 2012; Kochendorfer et al., 2020). Comprehending the characteristics of  
60 observational instruments and the data they produce is imperative to ensure the reliability of the research findings derived  
61 from observational data.

62 The standard instruments used to observe precipitation include rain gauges and disdrometers. A rain gauge measures the total  
63 precipitation accumulated over a specified time interval. In contrast, a disdrometer assesses the size and concentration of  
64 precipitation particles, thereby enabling the determination of the precipitation intensity and type. The selection of an  
65 appropriate type of rain gauge is contingent on specific observational objectives such as monitoring heavy rain, light rain, or  
66 snow. Notable examples of disdrometers include the Particle Size and Velocity (PARSIVEL), Two-dimensional Video  
67 Disdrometer (2DVD), Joss-Waldvogel Disdrometer, and Precipitation Occurrence Sensor System. Disdrometers compute the  
68 size-specific concentration of particles, known as the Drop Size Distribution (DSD), by analyzing the variations in optical  
69 intensity as the particles traverse the observation zone of the sensor. In contrast to data obtained from rain gauges,  
70 disdrometer data offer a broader range of applications because they provide physical parameters, such as particle number  
71 concentration and fall velocity, and morphological characteristics, such as oblateness.

72 A typical application of disdrometer data involves formulating Quantitative Precipitation Estimation (QPE) equations, which  
73 are used in conjunction with remote sensing data such as radar observations. To derive rainfall information from remote  
74 sensing data, researchers can leverage the correlation between rain rate and radar reflectivity values, an observational  
75 variable in remote sensing, to measure variations in rainfall (Ji et al., 2019; Tang et al., 2024). Additionally, DSD  
76 information obtained from disdrometer observations is instrumental in parameterizing microphysical schemes within  
77 numerical weather prediction models (Yang et al., 2019; Iversen et al., 2021). Microphysical schemes can be categorized  
78 into bin and bulk types (Hu and Igel, 2023). The bin scheme accurately simulates the distributional differences between  
79 hydrometeor types by accounting for their size-dependent number concentration. However, this approach is limited by its  
80 high computational demand and the need for substantial hardware resources during the simulation process. Consequently,  
81 bulk schemes are predominantly employed in weather prediction models. This approach simulates microphysical processes  
82 based on the relationships between particle diameter and concentration distributions for various hydrometeor types. The  
83 DSD model considerably influences the quantitative differences in the estimated precipitation property outcomes. As the  
84 reliability of the DSD model improves, so does the accuracy of the precipitation simulation and forecasting.

85 The DSD model used in the QPE and microphysical schemes of remote sensing encompasses various models, such as the  
86 Marshall-Palmer, exponential (Marshall and Palmer, 1948), and gamma models (Ulbrich, 1983). The configuration of each  
87 model is contingent on the specific parameters being analyzed, with the shape and slope variables in the DSD model varying  
88 according to the concentration distribution based on the particle diameter (Smith, 2003; Liu et al., 2021). The DSD is  
89 affected by several factors, such as the type of rainfall (Deo and Walsh, 2016), intensity of rainfall (Thomas et al., 2021), and  
90 climatological and topographical characteristics of the region where precipitation occurs and develops (Kim et al., 2022).  
91 Consequently, it is imperative to acquire DSD model parameters and reflectivity data by collecting highly reliable  
92 observational data that accurately represent precipitation characteristics to enhance the precision of rainfall estimations and  
93 simulations based on DSD. Furthermore, disdrometer data can be used to estimate rainfall erosivity (Serio et al., 2019).  
94 Enhancing the accuracy of rainfall erosivity estimates can facilitate the assessment of the impact of rainfall on soil erosion  
95 and serve as a foundation for developing countermeasures through spatial analysis and monitoring of soil erosion risk areas

96 using remote sensing data. Reliable precipitation observational data for estimating rainfall erosivity can aid in analyzing the  
97 effects of erosion resulting from alterations in rainfall patterns due to climate change.

98 Various quality control (QC) methods for disdrometer data have been suggested to enhance the accuracy of derived  
99 measurements (Kruger and Krajewski, 2002; Jaffrain and Berne, 2011; Raupach et al., 2015). QC approaches for  
100 disdrometer data primarily rely on the falling velocity of raindrops. In the absence of a substantial wind influence or particle  
101 collisions during descent, the fall velocity of a raindrop tends to increase with its diameter, ultimately reaching a terminal  
102 velocity. Terminal velocity is achieved when the forces of air resistance and gravitational pull are in equilibrium, resulting in  
103 no further particle acceleration (Wang and Pruppacher, 1977; Ong et al., 2021). Studies have been conducted to determine  
104 the terminal velocities of raindrop particles (Atlas et al., 1973; Beard, 1977; Brandes et al., 2002), which have led to the  
105 development of QC methods that use terminal velocity measurements. Kruger and Krajewski (2002) elucidated the structural  
106 design and operational principles of a 2DVD system, and noted that the recorded data indicated a fall velocity of  
107 approximately  $400 \text{ m s}^{-1}$ . However, this value is not feasible for raindrops. To mitigate the impact of erroneous data (outliers)  
108 potentially arising from hardware malfunctions, inaccuracies in data processing, and environmental conditions at the  
109 observation site, we employed a comparative analysis of the empirical relationship of raindrops established by Atlas et al.  
110 (1973). Furthermore, recognizing that the disdrometer may either underestimate or overestimate the fall velocity of  
111 precipitation particles influenced by the horizontal movement due to wind, this study conducted QC by focusing exclusively  
112 on the vertical velocity measurements. Jaffrain and Berne (2011) conducted a study to address the uncertainties associated  
113 with sampling observations from PARSIVEL disdrometers. They argued that the collected precipitation data exhibit inherent  
114 variability and measurement errors attributable to the equipment used, necessitating the development of a method to mitigate  
115 these issues and enhance data reliability. The authors proposed a method for eliminating anomalous data, such as outliers  
116 (values that are not physically plausible), instances of particle splashing (where the same particle is detected multiple times),  
117 and non-meteorological data. This preprocessing approach effectively diminished the sampling uncertainty of various  
118 parameters, including rain rate.

119 Raupach et al. (2015) conducted a study using data from the PARSIVEL and 2DVD to establish a correction factor for  
120 number concentration based on observations from the PARSIVEL disdrometer. The authors noted a tendency for  
121 PARSIVEL to overestimate the number of small droplets measuring between 0.2 and 0.4 mm and larger particles measuring  
122 2.4 mm or more. Furthermore, the measured fall velocity of larger droplets was lower than the actual terminal velocity.  
123 Anomalous data can lead to DSD distortions, which can compromise the accuracy of precipitation measurements and radar-  
124 based rainfall estimates. The focus of these studies was primarily on rainfall particles and it was determined that the  
125 quantitative accuracy of rainfall estimates improved when the aforementioned QC methods were applied across various  
126 environmental conditions.

127 Snow particles exhibit a variety of forms such as needles, dendrites, and granules, which are influenced by temperature and  
128 humidity. These variations in shape arise from the specific conditions under which the particles form and develop, leading to  
129 differences in their densities and fall velocities (Barthazy and Schefold, 2006; Vázquez-Martín et al., 2021). Furthermore,

서식 지정합: 글꼴 색 텍스트1

서식 지정합: 글꼴 색 텍스트1

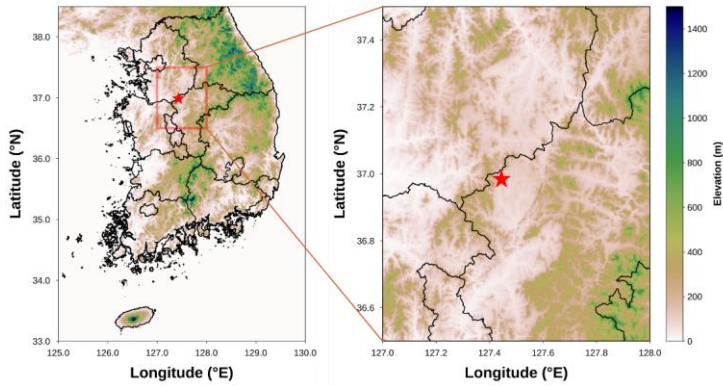
130 snow particles are more susceptible to wind because of their lower density and larger surface area than raindrops.  
131 Consequently, fall-velocity-based QC methods for eliminating non-meteorological particles (such as leaves, dust, and insects)  
132 are limited in their effectiveness because they primarily target solid particles with low fall velocities. Given the diverse  
133 shapes and fall speeds of snow particles, the mixing of raindrops and snow during precipitation events may lead to an  
134 underestimation of errors when applying conventional disdrometer QC methods. Therefore, it is imperative to establish  
135 objective criteria for differentiating rainfall and snowfall conditions to enhance the accuracy of rainfall analysis using  
136 disdrometer data. Ding et al. (2014) emphasized the significance of accurately classifying precipitation types for surface  
137 energy balance and hydrological process research. They aimed to develop a method for identifying precipitation types by  
138 analyzing 30 years of observational data. Their investigation focused on the correlation between precipitation type and  
139 various meteorological variables, including wet-bulb temperature ( $T_w$ ), relative humidity ( $RH$ ), and surface elevation. These  
140 findings indicate that using  $T_w$  as a reference variable for determining precipitation type is more reliable than relying on air  
141 temperature ( $T_{air}$ ). Furthermore, the proposed model, which incorporated  $T_w$ , demonstrated a determination accuracy  
142 exceeding 88%.

143 This study aims to evaluate the quantitative accuracy of rainfall measurements obtained from a disdrometer in relation to  
144 varying  $T_w$  conditions. Furthermore, this study seeks to establish environmental criteria to ensure the reliability of the  
145 parameters used in the DSD model by using long-term rainfall data collected through disdrometer observations. A  
146 comparative analysis of the disdrometer data was performed using different QC methods to examine the discrepancies  
147 between these methods under varying  $T_w$  conditions.

서식 지정합: 글꼴 색 텍스트1

## 148 **2 Data**

149 In this study, we evaluated the QC method applied to disdrometer data under varying precipitation conditions. To achieve  
150 this, we collected and analyzed regional observational data that accounted for the environmental factors associated with  
151 rainfall and snowfall. This study used data from a 2DVD installed at an observatory (Fig. 1) operated by the Weather Radar  
152 Center of the Korea Meteorological Administration. The integrity of the 2DVD data was corroborated through comparisons  
153 with measurements obtained from the tipping-bucket and weighing rain gauges. The analysis included observational data  
154 collected between January 2020 and February 2024.



155 **Figure 1: Location of ground observation station.**

156 **2.1 Disdrometer**

157 The 2DVD (Kruger and Krajewski, 2002) used for the validity analysis of the disdrometer was an optical disdrometer  
 158 developed by Joanneum Research. This instrument operates by projecting light through a bulb across a designated  
 159 observation area and capturing the intensity of the transmitted light using a camera positioned on the opposite side (Fig. 2).  
 160 When a particle, such as a raindrop, traverses the observation area (10 cm<sup>2</sup>) illuminated by the light sheet, its diameter is  
 161 determined by analyzing the reduction in the intensity and width of the light during its passage. Furthermore, the system  
 162 employs two cameras to observe the particles from orthogonal angles, allowing the fall velocity to be calculated based on the  
 163 differential height of the light sheet in the two orientations and time taken for the particles to descend. The 2DVD's  
 164 capability to acquire diameter and fall velocity data for individual particles offers superior temporal, dimensional, and  
 165 velocity resolution compared to traditional disdrometer data, which typically provide channel-based information. The  
 166 observational resolution of the camera was approximately 0.2 mm (512 pixels), making the particles smaller than the  
 167 indistinguishable threshold (Grazioli et al., 2014). For quantitative validation using rain gauge data, the output time  
 168 resolution was configured to one minute, with data classified at one-minute intervals.



169 **Figure 2: Two-dimensional video disdrometer.**

170 **2.2 Rain gauge**

171 Precipitation can occur in liquid droplets and solid particles, such as snow and graupel, when temperatures are at or near 0 °C.  
 172 To validate the disdrometer data under  $T_w$  conditions, an analysis was conducted using data from the tipping-bucket and  
 173 weighing-type rain gauges (Fig. 3). Each type of rain gauge offers an observational resolution of 0.1 mm and a temporal  
 174 resolution of 1 min. Both instruments were positioned within a 10 m radius of the 2DVD disdrometer.

(a) Tipping-bucket type



(b) Weighing type



175 **Figure 3: (a) Tipping-bucket rain gauge (0.1 mm) and (b) Weighing rain gauge (0.1 mm).**

### 176 3 Methods

177 Ding et al. (2014) argued that precipitation types such as rain, snow, and sleet co-occur when the  $T_{air}$  or  $T_w$  approaches or  
178 falls below 0 °C. They recommended using  $T_w$  as a more effective criterion for distinguishing between types of precipitation  
179 instead of relying solely on  $T_{air}$ . In this study, the temporal resolution of the temperature data differed from that of previous  
180 studies, which employed different temporal resolutions. To facilitate objective verification of the applicability of  $T_w$ ,  $T_{air}$  and  
181  $T_w$  were employed as criteria for classifying precipitation types, and a comprehensive analysis was conducted.

#### 182 3.1 Pre-processing of disdrometer data

183 A common QC approach for disdrometer data involves excluding non-meteorological data by analyzing fall velocity. In  
184 numerous studies ([Kruger and Krajewski, 2002](#); [Jaffrain and Berne, 2011](#); [Raupach and Berne, 2015](#); [Kim et al., 2019](#)), this  
185 QC process was implemented by establishing a threshold determined by the terminal velocity, as indicated in Eq. (1).

$$|V_{measured} - V_{ideal}| < C \times V_{ideal} \quad (1)$$

186 where  $V_{measured}$  and  $V_{ideal}$  represent the observed particle fall velocity (in  $m \cdot s^{-1}$ ) and empirical fall velocity (or terminal  
187 velocity), respectively. Constant  $C$  denotes the setting constant, which indicates the percentage of the terminal velocity. The  
188 proportion of the removed particles may fluctuate based on the value of  $C$ . Numerous previous studies have provided  
189 validation results using various setting constants. Studies that employed 2DVD data ([Kruger and Krajewski, 2002](#); [Thurai  
190 and Bringi, 2005](#); [Chang et al., 2009](#); [Wen et al., 2018](#)) predominantly adopted a setting constant of 0.4 (40%) during data  
191 processing. Studies that employed PARSIVEL data for analysis frequently applied a setting constant of 0.6, accounting for  
192 60% of the cases ([Jaffrain and Berne, 2011](#); [Friedrich et al., 2013](#); [Ji et al., 2019](#); [Kim et al., 2019](#)). Given that previous  
193 studies have encompassed various precipitation types, such as heavy rainfall, typhoons, orographic rainfall, and  
194 thunderstorms, the established 40% and 60% QC conditions can be regarded as reliable preprocessing criteria for rainfall  
195 events.

196 [Raupach and Berne \(2015\)](#) used data from a 2DVD instrument to derive correction factors for the drop-diameter channel in  
197 the PARSIVEL dataset. The fall velocity filtering technique employed for the 2DVD and PARSIVEL data involved the  
198 exclusion of particles exhibiting a terminal velocity exceeding  $4 m s^{-1}$ , as shown in Eq. (2), those with a fall velocity below  $3$   
199  $m s^{-1}$ , as indicated in Eq. (3), and those larger than  $7.5 mm$ , as shown in Eq. (4).

$$V_{measured} > V_{ideal} + 4 \quad (2)$$

$$V_{measured} > V_{ideal} - 3 \quad (3)$$

$$D > 7.5 \quad (4)$$

200 where  $D$  (in mm) is the diameter of the drop (or particle). This study involved a comparative analysis of the outcomes  
201 derived from the three QC methods based on fall velocity. Terminal velocity was determined using the equation established  
202 by [Atlas et al. \(1973\)](#) (Eq. (5)).

$$\Psi V_{ideal}(D) = 9.65 - 10.3 \exp(-0.6D) \quad (5)$$

서식 지정함: 글꼴 색 텍스트1

203 Three QC methods were used to evaluate the research findings. Methods 1 and 2 are used for the  $\pm 40\%$  and  $\pm 60\%$  ranges of  
 204 terminal velocity, respectively, whereas Method 3 is based on the approach proposed by Raupach and Berne (2015).  
 205 As the temperature decreased, various hydrometeors intermingled, resulting in a gradual reduction in the proportion of  
 206 raindrops. Current QC methods are capable of eliminating low-density snow particles; however, to quantitatively compare  
 207 and validate rainfall measurements obtained from rain gauge observations, particles that exhibit velocities below the  
 208 threshold established for raindrops in each QC method are categorized as solid meteorological particles. In addition, analyses  
 209 were conducted under the assumption that the solid particles melted and transformed into raindrops. This method aims to  
 210 evaluate data from tipping-bucket rain gauges, which may exhibit diminished quantitative accuracy as the proportion of solid  
 211 particles increases, and facilitate quantitative comparisons of rainfall observations derived from disdrometer data by  
 212 implementing the QC method as the temperature decreases.  
 213 The equivalent-melted diameter ( $D_{eq}$ ) at which a snow particle can transition into a raindrop while preserving its mass was  
 214 determined using Eq. (6), established by Delanoë et al. (2005). In this equation,  $\rho(D)$  ( $\text{g cm}^{-3}$ ) denotes the density of snow  
 215 particles as a function of their diameter, while  $\rho_w$  ( $\text{g cm}^{-3}$ ) denotes the density of water. The density of the snow particles was  
 216 computed based on the formula provided by Tiira et al. (2016) (Eq. (7)).

$$D_{eq} = \left( \frac{\rho(D)}{\rho_w} \right)^{1/3} D \quad (6)$$

$$\rho(D) = 0.226D^{-1.004} \quad (7)$$

### 217 3.2 Raindrop size distribution

218 The 2DVD data can be configured to correspond to user-defined diameter bin sizes, which in turn influence the  
 219 characteristics of the DSD output and the precision of the DSD model parameters (Marzuki et al., 2010). Consequently, this  
 220 study aims to facilitate the analysis of PASIVEL and 2DVD data for comparative purposes. To achieve this, 2DVD data  
 221 were processed using the diameter channel information derived from the PASIVEL data to compute the rain rate, number  
 222 concentration, and DSD model parameters. Detailed information regarding the diameter and velocity channels of the  
 223 PASIVEL data is provided in the appendices (Table A3-4). The rain rate ( $R$ ,  $\text{mm h}^{-1}$ ) is calculated using Eq. (8), which  
 224 incorporates the number concentration and fall velocity for each diameter. In determining the DSD model parameters after  
 225 the rain rate calculation, data from intervals where the rain rate was  $0.1 \text{ mm h}^{-1}$  or greater were considered, thereby  
 226 minimizing the uncertainty associated with the DSD model. The gamma model, recognized for its reliability in representing  
 227 DSD characteristics, was selected for analysis. This model (Eq. (9)) is characterized by the shape parameter  $\mu$  (Eq. (10)),  
 228 slope parameter  $\Lambda$  ( $\text{mm}^{-1}$ ) (Eq. (11)), and intercept parameter  $N_0$  ( $\text{mm}^{-1}\mu\text{m}^{-3}$ ) (Eq. (12)).

$$R = \frac{6\pi}{10^4} \int_{D_{min}}^{D_{max}} D^3 N(D) V(D) dD \quad (8)$$

$$N(D)_{gamma} = N_0 D^\mu \exp(-\Lambda D) \quad (9)$$

$$\mu = \frac{(7 - 11\eta) - [(7 - 11\eta)^2 - 4(\eta - 1)(30\eta - 12)]^2}{2(\eta - 1)} \quad (10)$$

$$\Lambda = \left[ \frac{M_2 \Gamma(\mu + 5)}{M_4 \Gamma(\mu + 3)} \right]^{1/2} = \left[ \frac{M_2(\mu + 4)(\mu + 3)}{M_4} \right]^{1/2} \quad (11)$$

$$N_0 = \frac{\Lambda^{(\mu+3)} M_2}{\Gamma(\mu + 3)} \quad (12)$$

229 The DSD parameters were derived from the  $n^{\text{th}}$  moment ( $M_n$ ), as indicated in Eq. (13), along with the  $\eta$  value, computed  
230 based on  $M_n$  as shown in Eq. (14).

$$M_n = \int_{D_{\min}}^{D_{\max}} D^n N(D) dD \quad (13)$$

$$\eta = \frac{\langle M_4 \rangle^2}{\langle M_2 \rangle \langle M_6 \rangle} = \frac{(\mu + 3)(\mu + 4)}{(\mu + 5)(\mu + 6)} \quad (14)$$

### 231 3.3 Wet-bulb temperature

232 Data from an Automatic Weather Station (AWS) installed at the observatory were used to compute the  $T_w$ . The  $T_{air}$  (in  
233 degrees Celsius) and  $RH$  (in percentages) values derived from the AWS observations were incorporated into the  $T_w$  (in  
234 degrees Celsius) calculation equation proposed by Stull (2011) (Eq. (15)) to determine the  $T_w$  value. The temporal resolution  
235 of  $RH$ ,  $T_{air}$ , and  $T_w$  was one minute, which was consistent with the temporal resolution of the disdrometer data.

$$T_w = T_{air} \operatorname{atan}\left[0.151977(RH + 8.313659)^{1/2}\right] + \operatorname{atan}(T_{air} + RH) - \operatorname{atan}(RH - 1.676331) \quad (15)$$

$$+ 0.00391838(RH)^{\frac{3}{2}} \operatorname{atan}(0.023101RH) - 4.686035$$

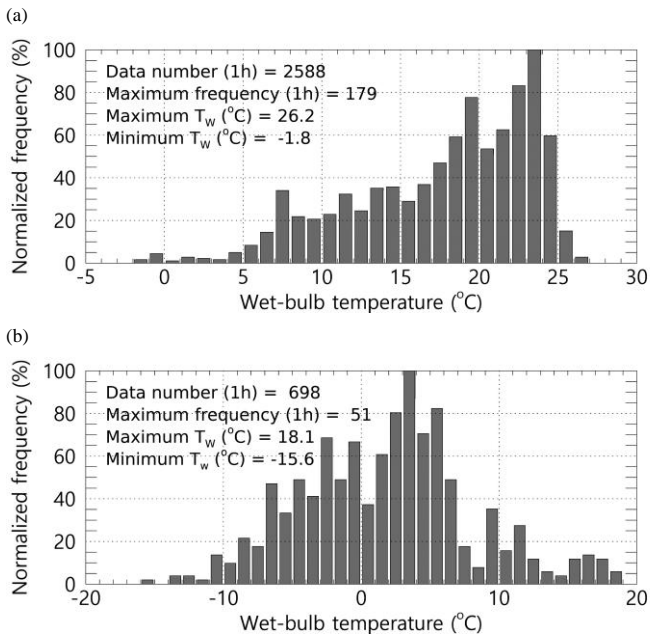
## 236 4 Results

### 237 4.1 Comparison of rainfall by the disdrometer pre-processing method

238 To validate the three QC methods employed for the disdrometer in this study, a comparative analysis was conducted between  
239 the rainfall measurements obtained from the disdrometer and those recorded by rain gauges. This comparison utilizes hourly  
240 accumulated rainfall data. Given that the QC methods for the disdrometer were specifically designed to address rainfall, the  
241 variable  $T_w$  was employed to differentiate between rainfall and snowfall, thereby facilitating the verification of **precipitation**  
242 **type** **rainfall-timing**. Ding et al. (2014) argued that snow is infrequently detected when  $T_w$  exceeds 5 °C. Figure 4 shows the  
243 distribution of  $T_w$  during the analysis period, specifically for instances when the hourly average  $T_w$  was either above or below  
244 5 °C. An examination of the one-minute  $T_w$  distribution during periods when the one-hour average  $T_w$  was 5 °C or higher  
245 (Fig. 4a) revealed a maximum  $T_w$  of 26.2 °C, with the highest proportion of values exceeding 20 °C. Conversely, the  
246 proportion of values falling below 5 °C was minimal, accounting for less than 5%. These findings suggest that it is feasible  
247 to delineate rainfall periods using the hourly average  $T_w$  as a reference when comparing hourly accumulated rainfall values.

서식 지정함: 글꼴 색 텍스트1

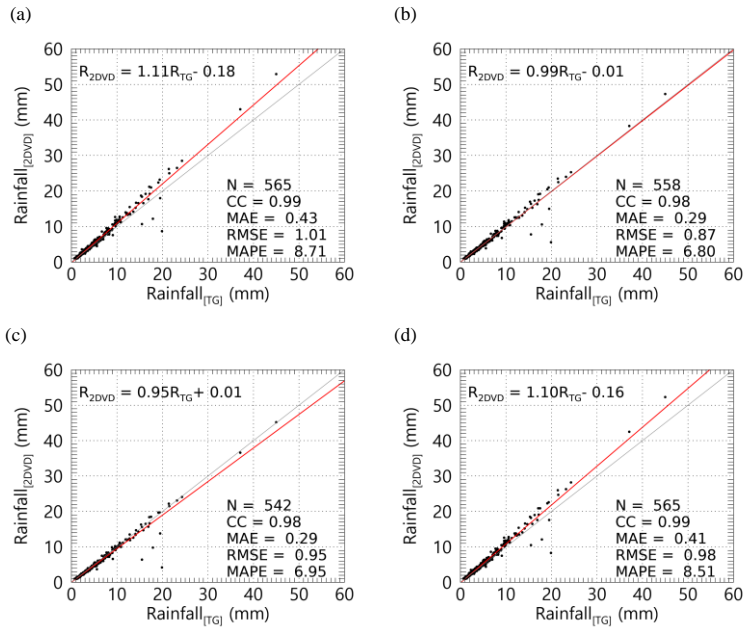
248 In contrast, the distribution of one-minute  $T_w$  during hours when the average  $T_w$  was below 5 °C exhibited a broad range,  
 249 with minimum and maximum  $T_w$  values exceeding 33 °C and a concentration of  $T_w$  values around 0 °C. This observation  
 250 indicates notable variability in  $T_w$  under 5 °C or lower, suggesting that the observational area encompasses environmental  
 251 conditions conducive to detecting diverse hydrometeors.



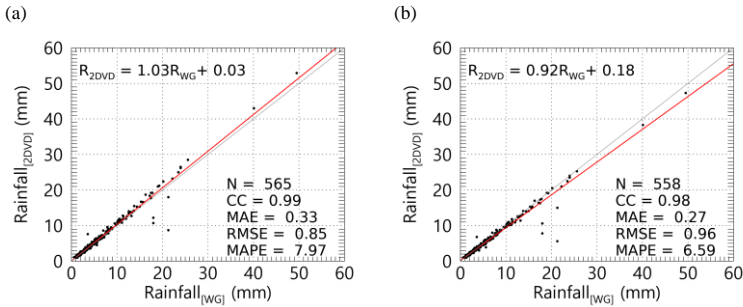
252 **Figure 4: Normalized frequency distribution of  $T_w$  during the analysis period (when the average hourly  $T_w$  is (a)  $T_w \geq 5$  °C, (b)  $T_w <$**   
 253 **5 °C).**

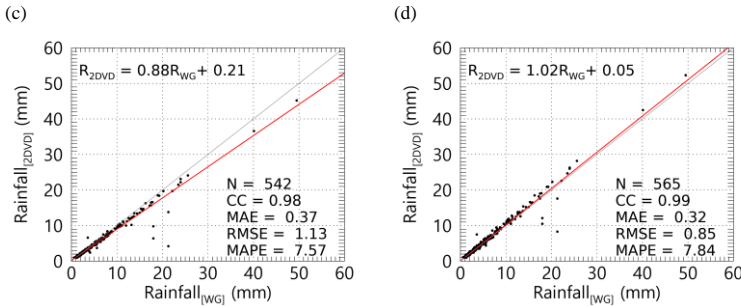
254 Figure 5-6 presents a comparative analysis of hourly rainfall measurements obtained from the tipping-bucket and weighing  
 255 rain gauge, specifically under conditions where the temperature ( $T_w$ ) equals or exceeds 5 °C, alongside data from the 2DVD  
 256 observations. The results derived from the unprocessed raw data were analyzed to evaluate the impact of the QC procedures.  
 257 The findings indicated a strong correlation, exceeding 0.98, between the 2DVD and rain gauge measurements, with a  
 258 regression line slope of approximately unity. However, the raw data tended to overestimate the 2DVD-derived rainfall  
 259 estimates compared to the QC-processed results. This discrepancy in the overestimation of the 2DVD data can be attributed  
 260 to variations in the conditions under which particles are eliminated, which is contingent on the specific QC method  
 261 employed. Following the application of the QC methods, the mean absolute percentage error (MAPE) demonstrated an

262 overall reduction compared with the raw data, suggesting that all QC methods possess quantitative reliability for rainfall data,  
 263 with a maximum reduction of approximately 2.1%.



264 **Figure 5: Comparison of rainfall observed using the tipping-bucket rain gauge and 2DVD when  $T_w \geq 5$  °C ((a) Unfiltered, (b)  
 265 Method 1, (c) Method 2, (d) Method 3).  $R_{2DVD}$  and  $R_{TG}$  denote the rainfall obtained from the 2DVD and a tipping-bucket rain  
 266 gauge, respectively.**





267 **Figure 6:** Comparison of rainfall observed using the weighing rain gauge and 2DVD when  $T_w \geq 5$  °C ((a) Unfiltered, (b) Method 1,  
268 (c) Method 2, (d) Method 3).  $R_{WG}$  denotes the rainfall obtained from a weighing rain gauge.

## 269 4.2 Fall velocity of particle by temperature and wet-bulb temperature

### 270 4.2.1 Fall velocity distribution at $T_{air}$ and $T_w$

271 Figure 7 shows the distribution of the fall velocity with the diameter of precipitation particles (raindrops) under varying  
272 conditions of  $T_w$  and  $T_{air}$ . When the  $T_w$  and  $T_{air}$  ranged from -1 to 04 °C, the fall velocity distributions were relatively  
273 comparable. However, as the temperature exceeded 0 °C, the fall velocity for CH 4 to 18 increased under  $T_w$  conditions,  
274 while under the  $T_{air}$  condition, it exhibited values similar to those observed at temperatures below 0 °C (Fig. 7(a-b)). When  
275  $T_w$  was below 0 °C, the upper 75% value of fall velocity was less than 2 m s<sup>-1</sup>. However, as  $T_w$  increased above 0 °C, fall  
276 velocity increased to approximately 1 m s<sup>-1</sup> or higher in the CH4–15 diameter range. Particularly in the CH8–11 range, the  
277 upper 75% value exceeded 3 m s<sup>-1</sup>. Specifically, up to CH13, the fall velocity gradually increased with diameter, reaching  
278 large values exceeding 6 m s<sup>-1</sup>. Conversely, under  $T_{air}$  conditions, the upper 75% fall velocity values for the CH1–15 range  
279 were 2 m s<sup>-1</sup> or less in the 0–1 °C range. Under  $T_{air}$  conditions, the fall velocity increased when the temperature was above  
280 1 °C. However, as the temperature exceeded 0 °C, the fall velocity for CH 4 to 18 increased under  $T_w$  conditions, while the  
281 fall velocity for CH 19 to 23 increased under  $T_{air}$  conditions (Fig. 7(a-b)). Notably, when the temperature rose above 1 °C,  
282 there was a notable increase in fall velocity; under  $T_w$  conditions, the distribution approached the terminal velocity of  
283 raindrops. Conversely, for diameters in the CH 12 or a higher range, the fall velocity remained at approximately 5.5 m s<sup>-1</sup>  
284 despite increases in diameter. Under  $T_{air}$  conditions, the fall velocity increased when temperatures were above/below 1 °C.  
285 However, it remained lower than that observed under  $T_w$  conditions, with a broader distribution of fall velocities across the  
286 diameter channels (Fig. 7(c)). At 2 °C or higher temperatures,  $T_w$  and  $T_{air}$  conditions yielded fall velocity distributions that  
287 were close to the terminal velocity of raindrops, with an increasing trend in distribution as temperature increased (Fig. 7(d-f)).  
288 However, under  $T_{air}$  conditions, the fall velocity was notably low, remaining below 2 m s<sup>-1</sup> for diameters of 3 mm (CH 17) or  
289 larger.

서식 지정함: 아래 첨자

서식 지정함: 글꼴 기울임꼴

서식 지정함: 글꼴 기울임꼴 아래 첨자

서식 지정함: 글꼴 기울임꼴

서식 지정함: 글꼴 기울임꼴 아래 첨자

서식 지정함: 위 첨자

서식 지정함: 글꼴 기울임꼴

서식 지정함: 글꼴 기울임꼴 아래 첨자

서식 지정함: 위 첨자

서식 지정함: 위 첨자

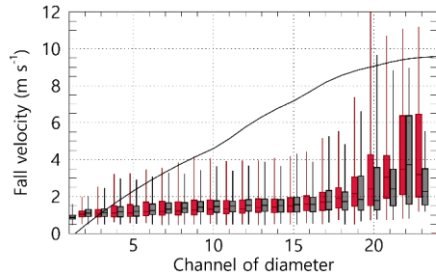
서식 지정함: 글꼴 기울임꼴

서식 지정함: 글꼴 기울임꼴 아래 첨자

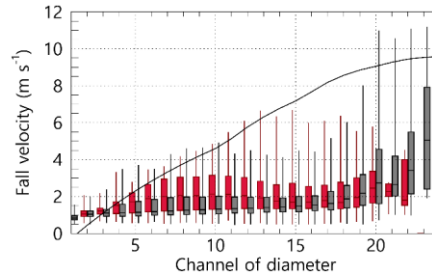
서식 지정함: 위 첨자

서식 지정함: 글꼴 색 해당

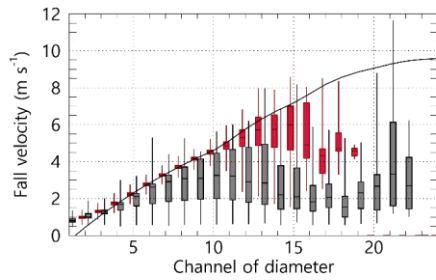
(a)  $-1\text{ }^{\circ}\text{C} \leq T_w (T_{air}) < 0\text{ }^{\circ}\text{C}$



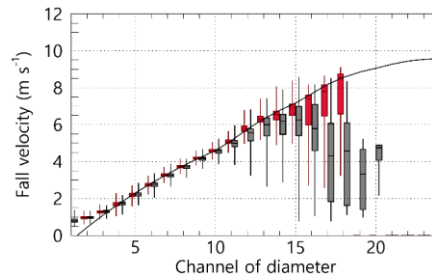
(b)  $0\text{ }^{\circ}\text{C} \leq T_w (T_{air}) < 1\text{ }^{\circ}\text{C}$



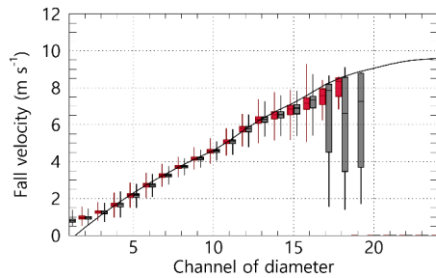
(c)  $1\text{ }^{\circ}\text{C} \leq T_w (T_{air}) < 2\text{ }^{\circ}\text{C}$



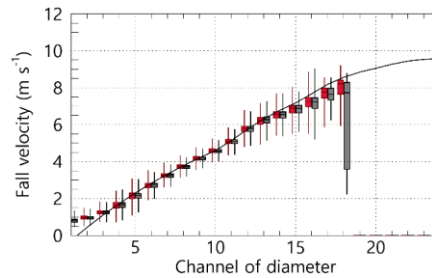
(d)  $2\text{ }^{\circ}\text{C} \leq T_w (T_{air}) < 3\text{ }^{\circ}\text{C}$



(e)  $3\text{ }^{\circ}\text{C} \leq T_w (T_{air}) < 4\text{ }^{\circ}\text{C}$



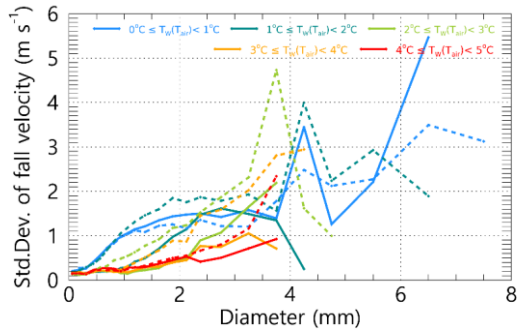
(f)  $4\text{ }^{\circ}\text{C} \leq T_w (T_{air}) < 5\text{ }^{\circ}\text{C}$



290 **Figure 7: Distribution of fall velocity by diameter channel based on  $T_w$  (red) and  $T_{air}$  (gray). The black solid line represents the**  
291 **terminal velocity of rain drops proposed by Atlas et al. (1973).**

292 Figure 8 shows the variability in fall velocity with respect to the changes in temperature. Notably, despite  $T_w$  and  $T_{air}$   
293 exhibiting similar numerical ranges, the distribution of fall velocity was considerably broader under  $T_{air}$  conditions. When  $T_w$   
294 exceeds  $3\text{ }^{\circ}\text{C}$ , the standard deviation across all diameter intervals remains low, approximately  $1\text{ m s}^{-1}$  or less. In instances

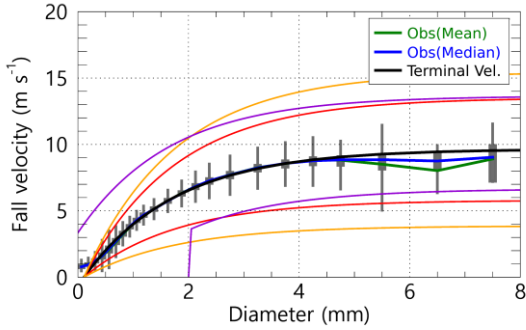
295 where  $T_w$  ranges between 2 and 3 °C, an increase in distribution is observed for diameters of 2.5 mm or greater, while the  
 296 standard deviation for diameters of 1 mm or more increases when  $T_w$  is between 1 and 2 °C. As temperature decreased, the  
 297 range of diameters exhibiting increased fall velocity variability progressively expanded. According to the findings under  $T_{air}$   
 298 conditions, the standard deviation of fall velocity for diameters exceeding 1 mm begins to rise below 4 °C, with values  
 299 surpassing 1 m s<sup>-1</sup> for diameters greater than 2 mm. The observation that when  $T_{air}$  is between 2 and 3 °C, the standard  
 300 deviation of fall velocity for diameters ranging from 3 to 4 mm is considerably increased, exceeding 2 m s<sup>-1</sup> and reaching up  
 301 to 4.5 m s<sup>-1</sup> is noteworthy. This broad fall velocity distribution suggests a mixture of various hydrometeors, complicating the  
 302 differentiation between rain and snow based solely on fall velocity. Consequently, subsequent analyses were conducted  
 303 using  $T_w$  as the criterion for distinguishing between rain and snow.



304 **Figure 8: Standard deviation of fall velocity by  $T_w$  (solid line) and  $T_{air}$  (dash line) range (1 °C interval).**

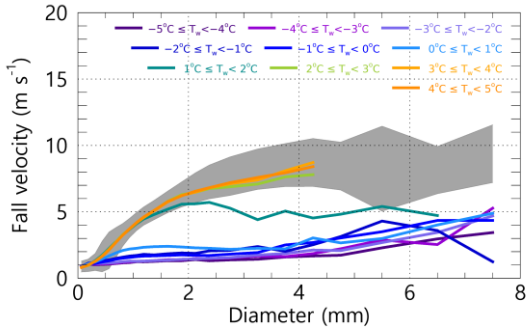
#### 305 4.2.2 Fall velocity distribution under rainfall condition

306 Figure 9 shows the distribution of fall velocities by diameter, derived from data collected when the  $T_w$  was at or above 5 °C.  
 307 The central value of the fall velocity is consistent with the terminal velocity. This is within the range of fall velocities for  
 308 raindrops, as established by the three different QC methods based on the fall velocity. It is important to note that  
 309 precipitation particles (drops) may experience variations in their fall velocities owing to factors such as wind influence or  
 310 collisions with obstacles during descent. The findings presented in Fig. 9 suggest that the observatory's measurements were  
 311 not considerably affected by wind or obstacles, thereby confirming the reliability of the velocity observation data of the  
 312 disdrometer.



313 **Figure 9:** Distribution of fall speed by diameter under conditions of  $T_w \geq 5$  °C, and effective fall velocity of raindrops by pre-  
 314 **processing methods (sky-blue The red (method 1), orange (method 2), and purple (method 3) solid lines represents the effective**  
 315 **velocity of raindrop applied to each QC method-Method 1, purple Method 2, and brown Method 3).**

316 An analysis of the fall velocity corresponding to temperature intervals ( $T_w$ ) of 1 °C revealed that when  $T_w$  is at or above 2 °C,  
 317 the fall velocities correspond with those typically observed for raindrops. Conversely, at  $T_w$  values between 1°C and 2 °C,  
 318 particles with diameters of 2 mm or less fall within the raindrop velocity range; however, as the diameter increases to 2 mm  
 319 or more, the fall velocity diminishes, stabilizing at approximately 5 m s<sup>-1</sup>. Temperature conditions ( $T_w$ ) may indicate a  
 320 mixture of raindrops and snow particles. At temperatures below 1 °C, the fall velocity of droplets with diameters of 4 mm or  
 321 less decrease to approximately 3 m s<sup>-1</sup>, exhibiting a low-velocity distribution of 5 m s<sup>-1</sup> or less across all diameter ranges.  
 322 This distribution suggests a higher proportion of solid (snow) particles when  $T_w$  is less than 1 °C.



323 **Figure 10:** Distribution of fall velocity by diameter in each  $T_w$  range. The grey area in the figure represents the Q1 (25%) – Q3  
 324 (75%) for the fall velocity by diameter when  $T_w \geq 5$  °C.

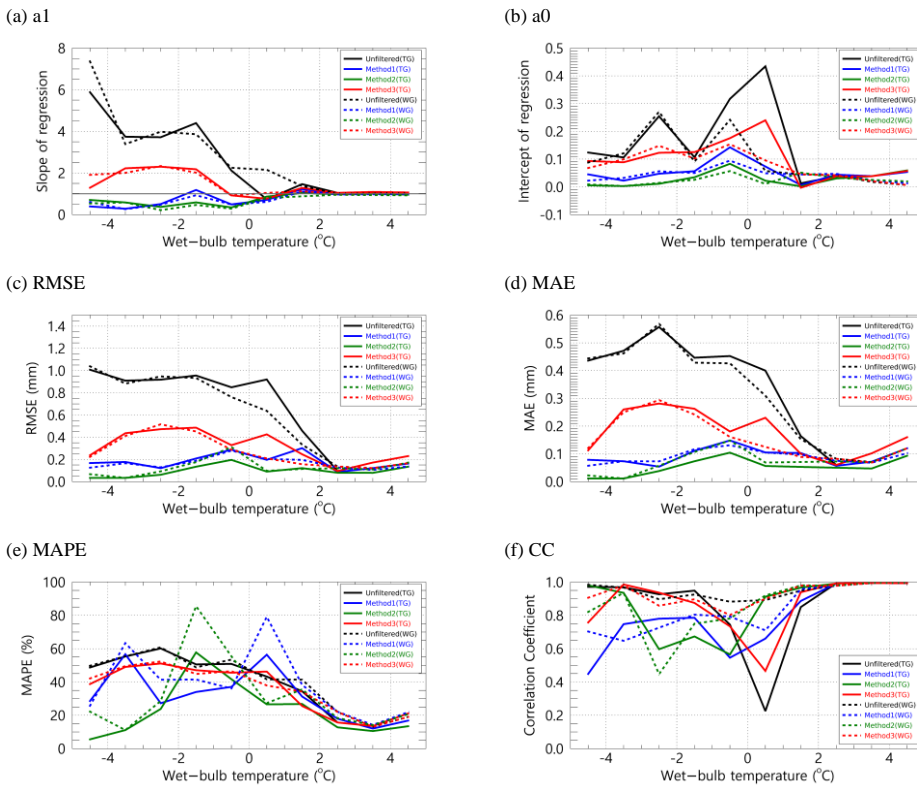
### 325 4.3 Accuracy of quantitative rainfall by wet-bulb temperature

326 Figures 11 and 12 show the outcomes of the comparative analysis and validation of rainfall measurements derived from the  
327 QC method applied to each  $T_w$  range, juxtaposed with the rainfall values obtained from a rain gauge. Figure 11 shows the  
328 results of applying the QC method, which effectively filtered out all particles except for raindrops. In contrast, Fig. 12  
329 depicts the assumption that the particles exhibiting low fall velocities are snow that melts and transforms into raindrops. The  
330 verification metrics employed in this analysis included the Root Mean Square Error (RMSE), Mean Absolute Error (MAE),  
331 MAPE, Correlation Coefficient (CC), slope ( $a_1$ ), and intercept ( $a_0$ ) derived from Eq. (14), which is the first-order regression  
332 equation correlating rainfall measurements from the rain gauge and 2DVD.

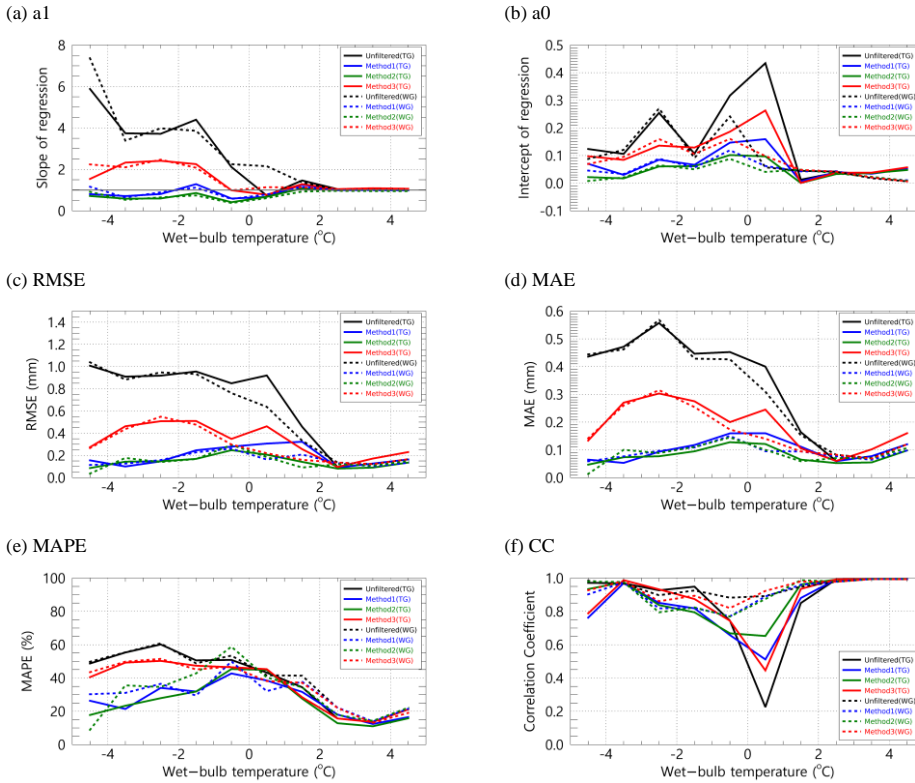
$$R_{2DVD} = a_1 R_{Gauge} + a_0 \quad (14)$$

333 The  $a_1$  of the observed relationship indicates that when the  $T_w$  exceeds 2 °C, the value remains close to one before and  
334 following the application of QC. However, as  $T_w$  drops below 2 °C, the value of  $a_1$  either increases or decreases. A value of  
335  $a_1$  greater than one suggests that the rainfall measurements derived from the 2DVD instrument tend to overestimate the  
336 corresponding values obtained from the rain gauge observations. In contrast, a value of less than one indicates an  
337 underestimation. Notably, in the absence of QC,  $a_1$  increases to two or more at temperatures below 0 °C, with the extent of  
338 overestimation intensifying as  $T_w$  decreases. This phenomenon is particularly evident when validated against a tipping-  
339 bucket rain gauge, where values of two or greater were recorded at temperatures ranging from 0 to 1 °C. This observation  
340 may be attributed to the different operational principles of the various rain gauge types within the specified  $T_w$  range (Fig.  
341 11a). At  $T_w$  below 0 °C, the unfiltered data and Method 3 exhibit  $a_0$  values exceeding one, while Method 2 and Method 3  
342 present  $a_1$  values below one. This discrepancy can be interpreted as a consequence of the varying quantities of preprocessed  
343 particles. For  $T_w$  values of 1 °C or higher,  $a_0$  is observed to range between 0 and 1; however, as  $T_w$  declines below 1 °C,  $a_0$   
344 experiences a rapid increase. Method 3, which uses a smaller filter area for unfiltered particles and those with diameters of 2  
345 mm or less, demonstrates  $a_0$  values of 0.2 or higher, exceeding those of Methods 1 and 2 (Fig. 11b).  
346 The CC decreases substantially in the  $T_w$  range, whereas  $a_0$  increases considerably (Fig. 11f). The RMSE and MAE were  
347 recorded at low values of less than 0.3 mm and 0.2 mm, respectively, when  $T_w$  was at or above 2 °C; however, these errors  
348 increased as  $T_w$  decreased to 1 °C or lower, with the magnitude of errors following the order of Unfiltered, Method 3,  
349 Method 1, and Method 2, which corresponds to the increasing trend of  $a_1$ . In the range of 0 to 2 °C, the errors associated with  
350 results validated by the tipping-bucket rain gauge were greater than those from the weighing rain gauge (Fig. 11(c-d)). The  
351 MAPE exhibited its lowest error rate, below 20%, at temperatures between 3 and 4 °C. It progressively increased with a  
352 decrease in  $T_w$ , ultimately reaching values of approximately 30% or more at temperatures of 2 °C or lower.  
353 Comparable findings were observed when it was assumed that the snow particles melted (Fig. 12), with an increase in error  
354 as the temperature ( $T_w$ ) dropped below 2 °C. The distinction between melted and unmelted snow particles was demonstrated  
355 using a weighing rain gauge as a verification tool. In scenarios where the melted state was disregarded at  $T_w$  values lower  
356 than 2 °C, the variability in the MAPE and CC was substantial, which was contingent upon fluctuations in  $T_w$ . Conversely,

357 the variability decreased when the melted state was considered, and the CC remained elevated approximately at 0.8 or above.  
 358 The pronounced escalation in error within the 0–1 °C range can be attributed to precipitation detected by the 2DVD system  
 359 that was not captured by the Tipping-bucket rain gauge (Fig. A1(f) in Appendix).  
 360 Furthermore, the low volatility and high correlation observed in the verification results using the weighing rain gauge within  
 361 the  $T_w$  range can be explained by incorporating raindrops and snow particles in the 0–1 °C range. By assuming melting of  
 362 snow particles, both forms of precipitation can be integrated into precipitation calculations. The weighing rain gauge  
 363 recorded precipitation values that accounted for the cumulative weight of all the raindrops and snow particles (Fig. A2(f) in  
 364 the Appendix).



365 **Figure 11: Quantitative comparison of rainfall from a rain gauge (The solid line represents the tipping-bucket and the dash line**  
 366 **represents the weighing rain gauge) and 2DVD by  $T_w$  (assuming that snow particles do not melt).**



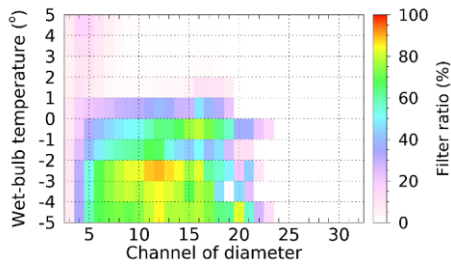
367 **Figure 12: Quantitative comparison of rainfall from a rain gauge (The solid line represents the tipping-bucket and the dash line**  
 368 **represents the weighing rain gauge) and 2DVD by  $T_w$  (assuming that snow particles melt).**

#### 369 4.4 Particle filter rate

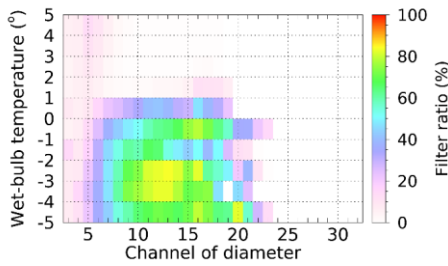
370 Precipitation measurements obtained from the disdrometer were derived from raindrop (or snow particle) accumulation. The  
 371 quantitative errors associated with these precipitation measurements were assessed by comparing the `filterremoval` rates of  
 372 raindrops (or snow particles) using the QC method. Figure 13 shows the `filterremoval` ratios corresponding to the  $T_w$  range  
 373 and channel diameter. The two methods, Method 1 and Method 2, exhibit differences in the range of removal velocities  
 374 based on particle diameter (see Fig. 9); specifically, Method 2 encompasses a broader spectrum of raindrop sizes compared  
 375 to Method 1, leading to an increased `filterremoval` rate when the  $T_w$  is below  $0^{\circ}\text{C}$ . Notably, the `filterremoval` rate for Method  
 376 2 surpasses that of Method 1 at temperatures lower than  $-2^{\circ}\text{C}$ . Conversely, Method 3 did not allow the removal of particles

377 smaller than 2 mm (as indicated in CH 14), regardless of their low fall velocity, resulting in a consistent **filterremoval** rate of  
378 0%, irrespective of variations in  $T_w$ . This suggests that the number of particles smaller than 2 mm may be greater in Methods  
379 1 and 2. Furthermore, the **filterremoval** rate was lower when snow particles were assumed to have melted than when they  
380 had not melted. Nonetheless, for particles with a diameter of 1 mm or less, the **filterremoval** rate ranged from approximately  
381 10% to 30% when  $T_w$  exceeded 1 °C, which appears to be attributable to the removal of particles exhibiting a fall velocity  
382 that exceeds the raindrops.

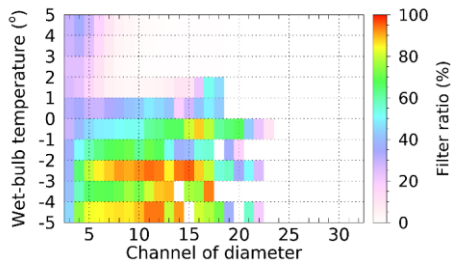
(a) Method 1



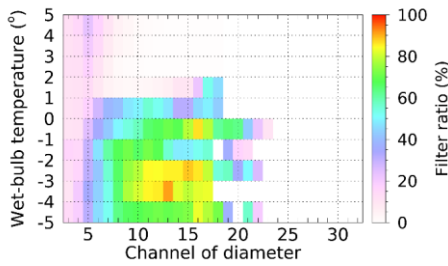
(b) Method 1 (melted)



(c) Method 2

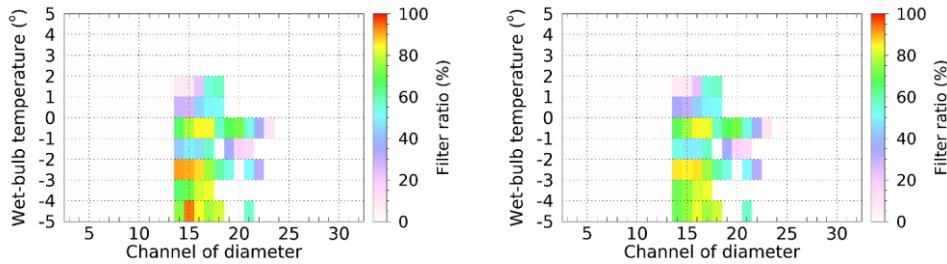


(d) Method 2 (melted)



(e) Method 3

(f) Method 3 (melted)



383 **Figure 13: Particle filter ratio by diameter channel for  $T_w$  according to the pre-processing method based on falling velocity.**

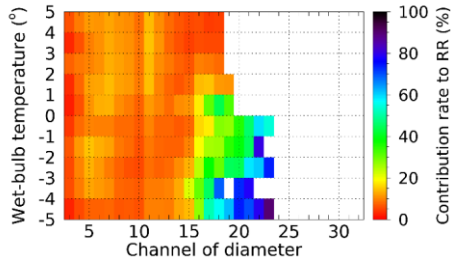
#### 384 4.5 Contribution rate by particle diameter to precipitation intensity

385 Figure 14 shows the contribution rate of the number concentration by diameter to the precipitation intensity as derived from  
 386 the disdrometer data. It is observed that when the  $T_w$  exceeds 1 °C, the contribution rate remains approximately 20% or lower  
 387 across all diameters. Conversely, when  $T_w$  is below 1 °C, the concentration of particles measuring 3 mm (CH 15) or larger  
 388 considerably influences the calculation of precipitation intensity. The contribution rate of 1.25 to 1.75 mm diameter (CH 11  
 389 to 13) decreased when the temperature was lower than 1 °C. The decrease in the contribution rate of drops smaller than 3  
 390 mm and the increase in the contribution rate of larger drops was as a result of the decrease in the concentration of drops  
 391 smaller than 3 mm through the QC process (Section 4.4), which increased the impact of relatively larger drops on the  
 392 calculation of precipitation intensity. This phenomenon can be attributed to the direct proportionality of the precipitation  
 393 intensity to  $N(D)$  and  $D^3$ , indicating that an increase in the particle diameter substantially affected the results. After QC, a  
 394 substantial increase in the contribution rate for a specific diameter may affect the precipitation intensity owing to a decrease  
 395 in the concentration of drops in the diameter range with a lower contribution rate.

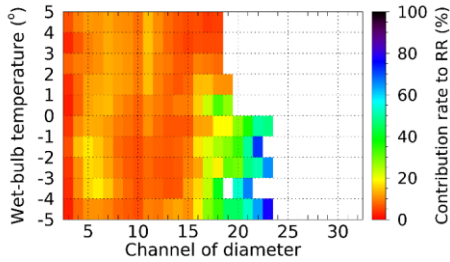
396 In scenarios where it is assumed that snow particles have melted, the diameter of these particles decreases, increasing the  
 397 concentration of smaller particles. As a result, the contribution rate of diameter from approximately 0.5 to 1 mm (CH 5 to 10)  
 398 increased. Notably, in Method 3, there was a minimal removal of particles smaller than 2 mm, which resulted in negligible  
 399 differences between the scenarios that accounted for the melted state of snow particles and those that did not.

(a) Method 1

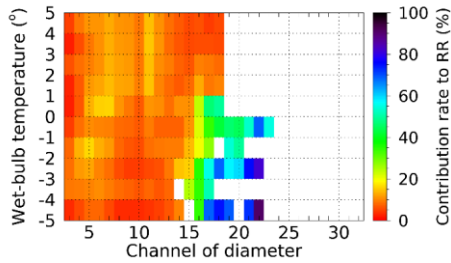
(b) Method 1 (melted)



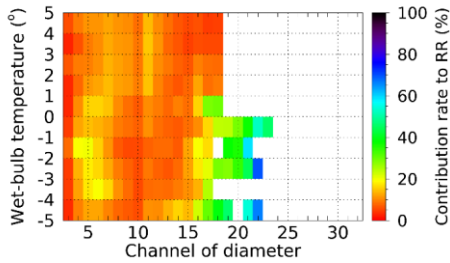
(c) Method 2



(d) Method 2 (melted)



(e) Method 3



(f) Method 3 (melted)

400 **Figure 14: Precipitation contribution rate by diameter channel for  $T_w$  using the pre-processing method based on falling velocity.**

401 **4.6 Drop size distribution**

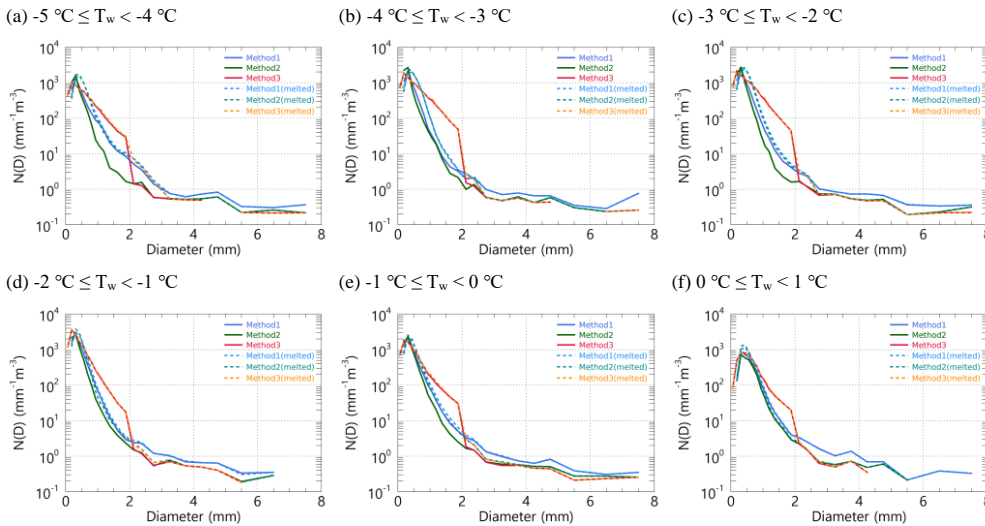
402 **4.6.1 Number concentration calculated by applying QC methods based on  $T_w$**

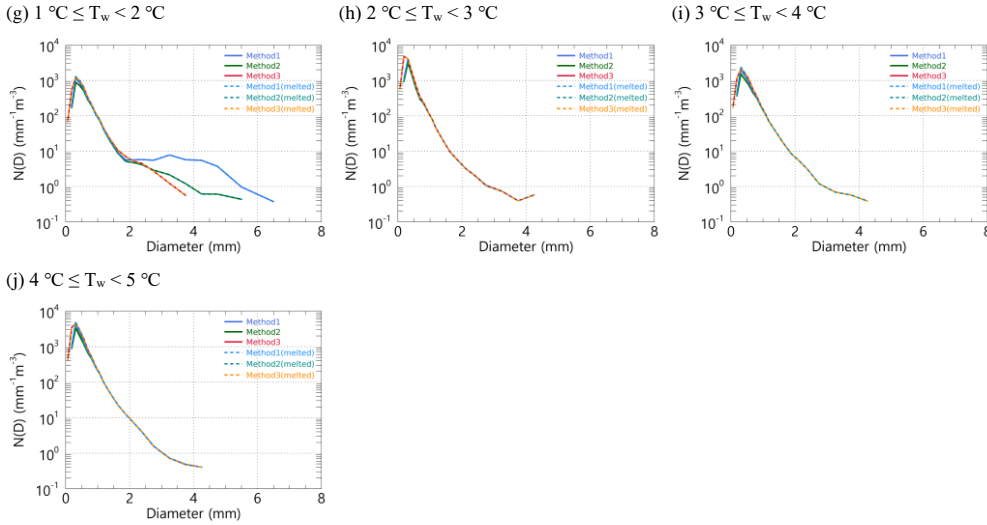
403 The precipitation intensity derived from disdrometer data is contingent on the number concentration; therefore, examining  
 404 the distribution of the number concentration is imperative. Figure 15 shows the average distribution of the number

405 concentration obtained by applying the QC method under varying  $T_w$  conditions. Notably, when the temperature exceeded  
 406 2 °C, the distributions yielded by all QC methods were comparable. Method 3 exhibited a relatively high concentration of  
 407 small droplets measuring 1 mm or less, whereas the number of droplets measuring 1 mm or more showed minimal variation  
 408 (Fig. 15h). This finding indicates that, at temperatures above 2 °C, the output values remain consistent across different QC  
 409 methods.

410 At temperatures ranging from 1 to 2 °C, the distribution of particles exceeding 2 mm in size was distinctly differentiated  
 411 according to the QC method employed. This finding suggests that the fall velocity of particles larger than 2 mm exhibits  
 412 considerable variation within this temperature interval (Fig. 10). Conversely, at temperatures below 1 °C, the distribution  
 413 obtained through Method 3 displayed an anomalous pattern. This irregularity can be attributed to the failure of Method 3 to  
 414 exclude snow particles smaller than 2 mm, leading to a higher concentration than that of the other QC methods. When  
 415 considering the scenario in which particles are assumed to have melted, an increase in the concentration of water was  
 416 observed for particles with a diameter of 1 mm or less when the  $T_w$  was between 0 and 1 °C, while the concentration of  
 417 particles larger than 2 mm remained relatively unchanged.

418 In comparing scenarios where particles are assumed to have melted versus those that are not, no notable differences were  
 419 observed at temperatures exceeding 1 °C (see Fig. 15g). However, within the temperature range of 0 to 1 °C, there was an  
 420 increase in the number of particles smaller than 1 mm. There was a similar distribution in the number of medium and larger  
 421 particles (1 mm or more). As the  $T_w$  progressively decreased below 0 °C, the disparity in the number concentration of  
 422 particles larger than 1 mm became more pronounced (Fig. 15(a-e)).





423 **Figure 15: Average number concentration distribution for  $T_w$  using pre-processing methods.**

#### 424 4.6.2 Difference in the number concentration based on the gamma model

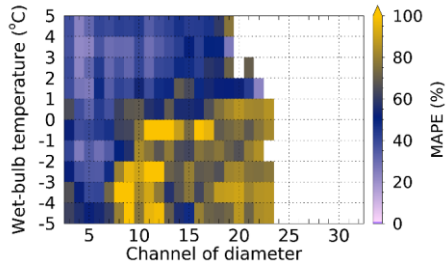
425 The change in the shape of the number concentration within the observed data has implications for DSD model parameters.  
 426 The notable discrepancy between the observed number concentration and that derived from the model parameters raises  
 427 concerns regarding the reliability of the DSD model.

428 Figures 16 and 17 show the variance between the observed number concentration and that predicted using the gamma model.  
 429 When all QC methods were implemented, the MAPE remained below 60% across all diameter ranges at temperatures  
 430 exceeding 2 °C. However, as the  $T_w$  fell below 1 °C, the discrepancy for diameters greater than 0.6 mm (CH 7) escalated to  
 431 over 70%. At 2 °C or higher temperatures, the gamma distribution overestimated the concentration of particles smaller than 1  
 432 mm while underestimating those larger than 1 mm. Nonetheless, the extent of under- or over-simulation by gamma  
 433 distribution remained below 50% across all diameter intervals.

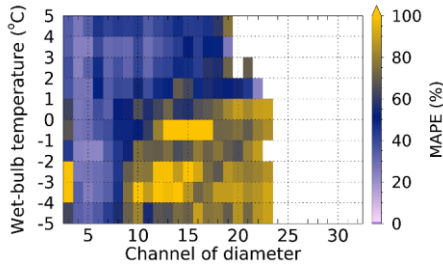
434 When  $T_w$  was below 1 °C, assuming that the snow particles had melted, the error rate in simulating the concentration of  
 435 particles smaller than 1 mm (CH 8) diminished (Fig. 16(b, d)). Concurrently, the percentage bias (PBAIS) for particle  
 436 diameters less than 1 mm decreased, approaching a value near zero (Fig. 17(b, d)). This phenomenon can be attributed to the  
 437 application of the QC method under subzero conditions, which led to an overestimation of the gamma distribution for  
 438 diameters of 1 mm or less because of the increased influence of smaller particles resulting from the exclusion of larger

439 particles exceeding 3 mm. Conversely, this resulted in an underestimation of the gamma distribution for diameters larger  
440 than 3 mm.

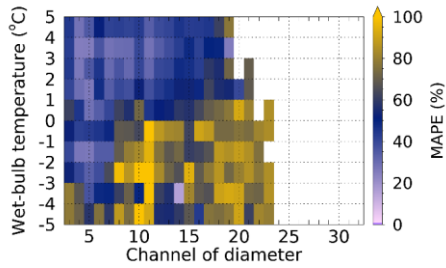
(a) Method 1



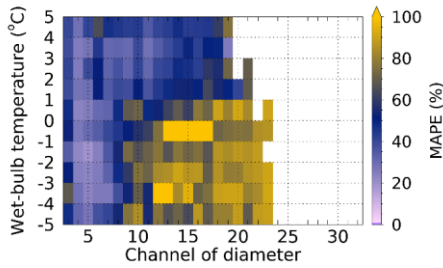
(b) Method 1 (melted)



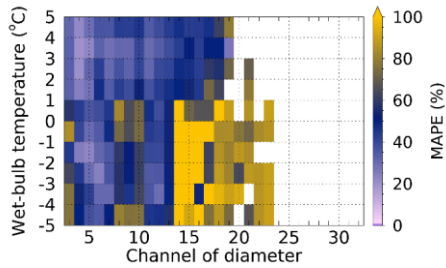
(c) Method 2



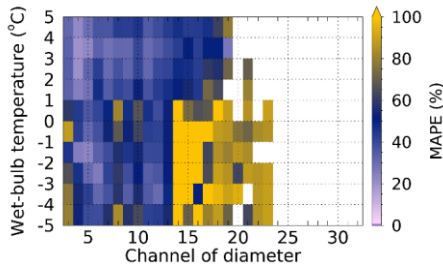
(d) Method 2 (melted)



(e) Method 3



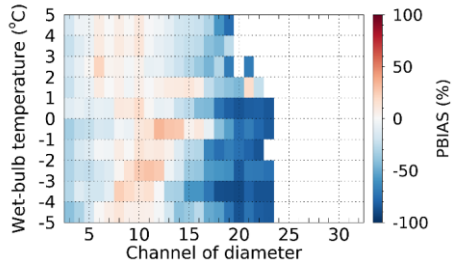
(f) Method 3 (melted)



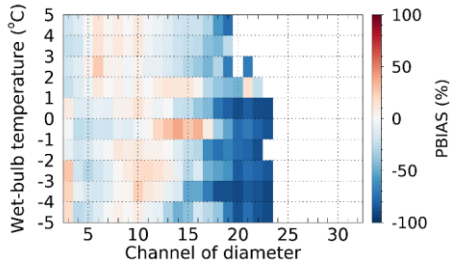
441 **Figure 16: MAPE for diameter and wet-bulb temperature using the pre-processing method**

(a) Method 1

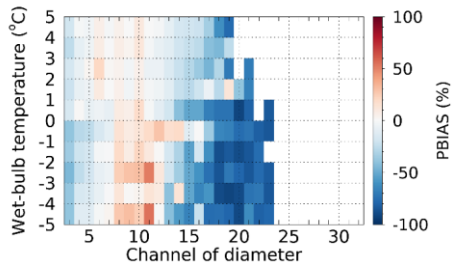
(b) Method 1 (melted)



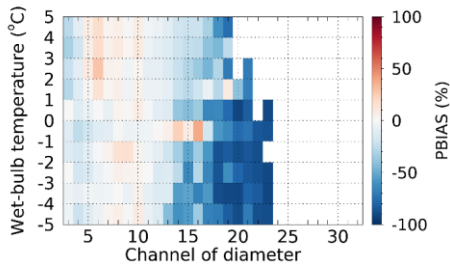
(c) Method 2



(d) Method 2 (melted)



(e) Method 3



(f) Method 3 (melted)

442 **Figure 17: PBAIS for diameter and wet-bulb temperature using the pre-processing method**

443 **5 Conclusion**

444 This study employed data collected from a 2DVD disdrometer in conjunction with traditional rain gauges to assess the  
 445 precipitation measurements derived from the disdrometer under  $T_w$  conditions and to evaluate the reliability of the DSD  
 446 model.

447 The precipitation estimates derived from the QC methods employed in this study exhibited  $CC \geq 0.98$  when juxtaposed with  
448 precipitation measurements obtained from rain gauges in an environment with  $T_w$  of 5 °C higher. The MAPE was  
449 approximately 8.5%. In contrast to scenarios in which the QC method was not implemented, the propensity for the 2DVD  
450 data to be overestimated diminished, and the overall error rate reduced. These findings indicate that all QC methods  
451 demonstrated high reliability under rainfall conditions.

452 When  $T_{air}$  and  $T_w$  dropped below 1 °C, there was a notable reduction in the fall velocity of precipitation particles, which  
453 became concentrated within a velocity range of approximately 0.5 to 3 m s<sup>-1</sup>. Moreover, the ratio of snow particles to  
454 raindrops considerably increased at temperatures below 1 °C for  $T_{air}$  and  $T_w$ . This observation is consistent with the findings  
455 of Ding et al. (2014), which indicated that the proportion of rain was less than 30% at temperatures below this threshold.  
456 Conversely, when  $T_{air}$  ranged from 1 to 3 °C, the distribution of fall velocities exhibited a broader range compared to  
457 conditions where  $T_w$  was between 1 and 3 °C, resulting in a greater disparity with the terminal velocity of raindrops.  
458 Consequently, it is justifiable to use  $T_w$  as a reference parameter to differentiate between types of precipitation using  
459 disdrometer data.

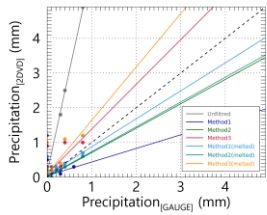
460 The fall velocity of particles exceeding 2 mm in diameter decreased within the 1 to 2 °C temperature range for  $T_w$ .  
461 Conversely, at  $T_w$  below 1 °C, the observed results were outside the effective fall velocity range typically associated with  
462 raindrops. Furthermore, as  $T_w$  decreased below 2 °C, the quantitative error, as measured by the correlation of disdrometer-  
463 based precipitation data, increased. These results can be attributed to the fact that the filter ratio for particles measuring 3  
464 mm or less escalated to 30% or higher when  $T_w$  was below 2 °C. Within this  $T_w$  range, it is plausible to regard raindrops and  
465 solid particles as intermixed; consequently, implementing QC methods appropriate for conventional rainfall scenarios may  
466 lead to inaccuracies. However, when snow particles were assumed to have undergone melting, the correlation approached  
467 0.9, even within the temperature range of 0 to 1 °C, and the variability of the error decreased. These findings indicate that the  
468 reliability of precipitation calculations can be maintained, even in scenarios where raindrops and snow particles coexist at  
469 temperatures between 0 and 2 °C, provided that an appropriate density for snow particles is used. Additionally, it is  
470 recommended that a weighing rain gauge be employed to verify precipitation when  $T_w$  is below 2 °C.

471 At 2 °C or higher  $T_w$ , the DSD shape remained consistent across different QC methods. However, as the temperature dropped  
472 below 2 °C, Method 1, which defines the raindrop size interval as  $\pm 40\%$  of the terminal velocity, indicated a comparatively  
473 elevated number of drops measuring 2 mm or larger. In conditions where the temperature was below 1 °C, the application of  
474 Method 3 (Raupach et al., 2015) resulted in a notable and irregular distribution of number concentration for droplet  
475 diameters ranging from 1 to 2 mm. These findings can be attributed to the QC method employed, which raises concerns  
476 about the reliability of the DSD parameters derived from the altered shape of the DSD. Consequently, it is imperative to use  
477 disdrometer data corresponding to environmental conditions with temperatures of 2 °C or higher when calculating DSD  
478 parameters and DSD-based rain rates.

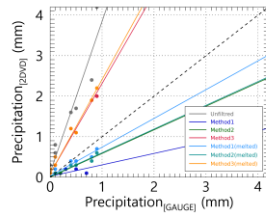
479 **Appendices**

480 Figures A1 and A2 present the findings from a comparative analysis of hourly accumulated precipitation intensity, derived  
 481 from observations using the 2DVD and two types of rain gauges (A1 represents the tipping-bucket type and A2 represents  
 482 the weighing type) under the specified  $T_w$  interval conditions at 1 °C intervals. In each figure, the solid line denotes the  
 483 regression line correlating the precipitation intensities derived by applying each quality control (QC) method. The constants  
 484 and validation indices associated with the regression lines are listed in Tables A1 and A2, respectively. Tables A3 and A4  
 485 provide details regarding the diameter and velocity channels used to calculate the number concentration based on 2DVD data.  
 486 The channel information corresponded to the values employed in the PARSIVEL disdrometer data.

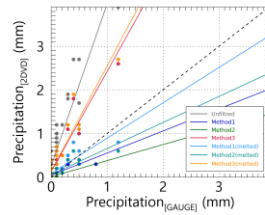
(a)  $-5\text{ °C} \leq T_w < -4\text{ °C}$



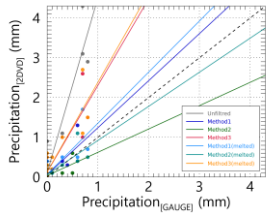
(b)  $-4\text{ °C} \leq T_w < -3\text{ °C}$



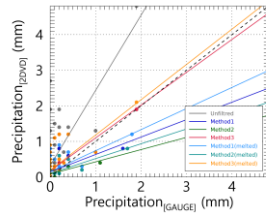
(c)  $-3\text{ °C} \leq T_w < -2\text{ °C}$



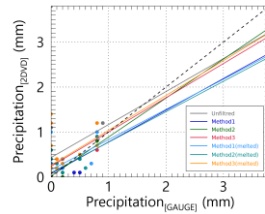
(d)  $-2\text{ °C} \leq T_w < -1\text{ °C}$



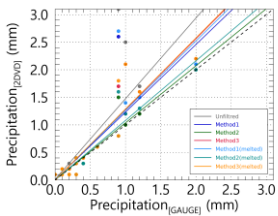
(e)  $-1\text{ °C} \leq T_w < 0\text{ °C}$



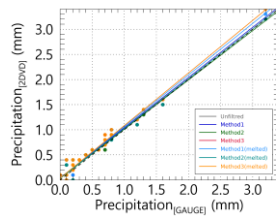
(f)  $0\text{ °C} \leq T_w < 1\text{ °C}$



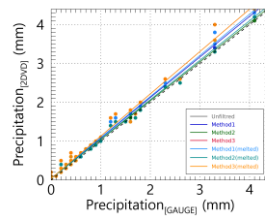
(g)  $1\text{ °C} \leq T_w < 2\text{ °C}$



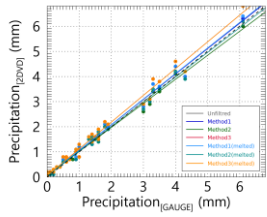
(h)  $2\text{ °C} \leq T_w < 3\text{ °C}$



(i)  $3\text{ °C} \leq T_w < 4\text{ °C}$

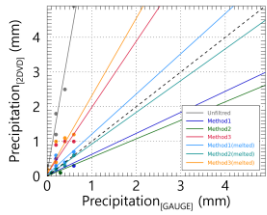


(j)  $4\text{ °C} \leq T_w < 5\text{ °C}$

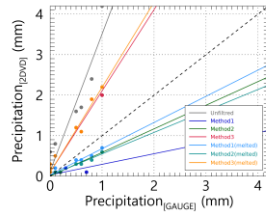


487 **Figure A1: Precipitation intensity scatter plot based on tipping-bucket rain gauge and 2DVD observation data for each  $T_w$  range.**  
 488 Each color in the scatter plot represents a filtering method.

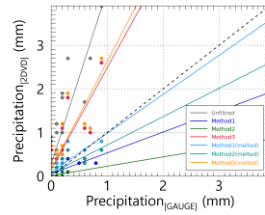
(a)  $-5\text{ }^{\circ}\text{C} \leq T_w < -4\text{ }^{\circ}\text{C}$



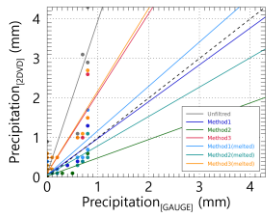
(b)  $-4\text{ }^{\circ}\text{C} \leq T_w < -3\text{ }^{\circ}\text{C}$



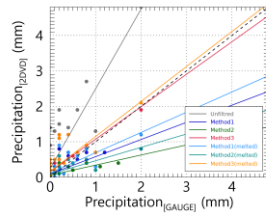
(c)  $-3\text{ }^{\circ}\text{C} \leq T_w < -2\text{ }^{\circ}\text{C}$



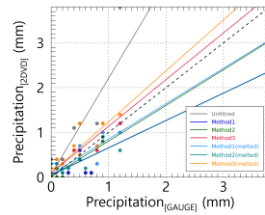
(d)  $-2\text{ }^{\circ}\text{C} \leq T_w < -1\text{ }^{\circ}\text{C}$



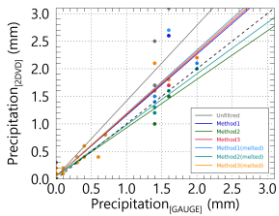
(e)  $-1\text{ }^{\circ}\text{C} \leq T_w < 0\text{ }^{\circ}\text{C}$



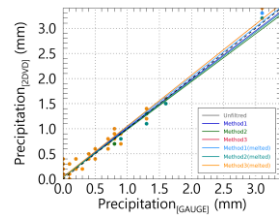
(f)  $0\text{ }^{\circ}\text{C} \leq T_w < 1\text{ }^{\circ}\text{C}$



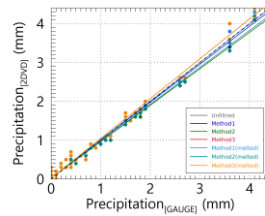
(g)  $1\text{ }^{\circ}\text{C} \leq T_w < 2\text{ }^{\circ}\text{C}$



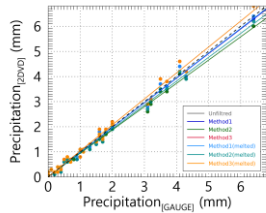
(h)  $2\text{ }^{\circ}\text{C} \leq T_w < 3\text{ }^{\circ}\text{C}$



(i)  $3\text{ }^{\circ}\text{C} \leq T_w < 4\text{ }^{\circ}\text{C}$



(j)  $4\text{ }^{\circ}\text{C} \leq T_w < 5\text{ }^{\circ}\text{C}$



489 **Figure A2:** Precipitation intensity scatter plot based on weighing rain gauge and 2DVD observation data for each  $T_v$  range. Each  
 490 color in the scatter plot represents a filtering method.

491 **Table A1:** Comparison of precipitation intensity based on tipping-bucket rain gauge and 2DVD observation data for each  $T_v$  range.

		T1	T2	T3	T4	T5	T6	T7	T8	T9	T10
Unfiltered	$a_I$	5.88	3.74	3.72	4.40	2.11	0.73	1.46	1.05	1.09	1.06
	$a_0$	0.12	0.11	0.25	0.11	0.32	0.43	0.01	0.04	0.04	0.06
	RMSE	1.01	0.91	0.92	0.96	0.85	0.92	0.46	0.10	0.17	0.23
	MAE	0.44	0.47	0.56	0.45	0.45	0.40	0.16	0.06	0.10	0.16
	MAPE	48.71	55.32	60.15	50.58	50.86	43.25	34.45	15.68	13.54	21.14
	CC	0.97	0.97	0.93	0.95	0.74	0.23	0.85	0.99	0.99	0.99
Method 1	$a_I$	0.39	0.28	0.51	1.18	0.49	0.71	1.23	1.00	1.04	1.01
	$a_0$	0.04	0.02	0.05	0.06	0.14	0.07	0.01	0.04	0.04	0.05
	RMSE	0.17	0.18	0.12	0.21	0.29	0.20	0.30	0.09	0.12	0.16
	MAE	0.08	0.07	0.05	0.11	0.15	0.11	0.10	0.06	0.07	0.12
	MAPE	28.57	56.67	27.24	34.01	37.07	56.39	31.27	17.96	12.04	16.83
	CC	0.45	0.75	0.78	0.79	0.55	0.66	0.89	0.99	1.00	0.99
Method 2	$a_I$	0.70	0.58	0.37	0.59	0.34	0.87	1.03	0.98	1.00	0.96
	$a_0$	0.01	0.00	0.01	0.03	0.08	0.02	0.00	0.03	0.04	0.06
	RMSE	0.03	0.03	0.06	0.13	0.20	0.09	0.12	0.08	0.08	0.13
	MAE	0.01	0.01	0.04	0.07	0.10	0.06	0.05	0.05	0.05	0.09
	MAPE	5.56	11.11	23.81	57.78	41.67	26.56	26.79	12.78	10.54	13.44
	CC	0.98	0.94	0.60	0.67	0.57	0.91	0.97	0.99	1.00	1.00
Method 3	$a_I$	1.29	2.22	2.30	2.18	0.92	0.76	1.28	1.05	1.09	1.06
	$a_0$	0.09	0.09	0.12	0.13	0.18	0.24	0.00	0.04	0.04	0.06
	RMSE	0.24	0.44	0.47	0.49	0.33	0.43	0.25	0.10	0.17	0.23
	MAE	0.11	0.26	0.28	0.26	0.18	0.23	0.10	0.06	0.10	0.16
	MAPE	38.75	49.04	51.11	47.07	45.58	46.25	25.58	15.68	13.54	21.14

	CC	0.76	0.99	0.94	0.87	0.73	0.47	0.94	0.99	0.99	0.99
Method 1 (melted)	$a_I$	0.81	0.71	0.81	1.29	0.59	0.67	1.26	1.03	1.06	1.02
	$a_0$	0.07	0.03	0.08	0.07	0.15	0.16	0.01	0.04	0.03	0.05
	RMSE	0.16	0.10	0.15	0.25	0.28	0.31	0.32	0.09	0.13	0.16
	MAE	0.06	0.05	0.09	0.12	0.16	0.16	0.11	0.06	0.08	0.12
	MAPE	26.33	21.39	34.06	31.87	42.73	38.50	31.64	18.03	12.37	16.51
	CC	0.76	0.97	0.85	0.82	0.66	0.51	0.88	0.99	1.00	0.99
Method 2 (melted)	$a_I$	0.71	0.59	0.60	0.86	0.42	0.68	1.08	0.99	1.02	0.98
	$a_0$	0.02	0.02	0.06	0.06	0.10	0.10	0.00	0.03	0.04	0.05
	RMSE	0.09	0.14	0.15	0.17	0.25	0.21	0.14	0.08	0.09	0.13
	MAE	0.05	0.07	0.08	0.09	0.13	0.12	0.06	0.05	0.05	0.10
	MAPE	17.78	23.33	27.88	31.87	45.37	44.88	27.62	12.84	11.00	15.80
	CC	0.93	0.98	0.84	0.79	0.67	0.65	0.96	0.99	1.00	1.00
Method 3 (melted)	$a_I$	1.54	2.33	2.41	2.25	0.99	0.77	1.29	1.05	1.09	1.06
	$a_0$	0.10	0.08	0.14	0.13	0.19	0.26	0.00	0.04	0.04	0.06
	RMSE	0.27	0.46	0.51	0.51	0.35	0.46	0.26	0.10	0.17	0.23
	MAE	0.13	0.27	0.30	0.28	0.20	0.25	0.11	0.06	0.10	0.16
	MAPE	40.50	49.24	50.27	47.38	46.46	45.30	28.44	15.68	13.54	21.14
	CC	0.79	0.99	0.93	0.87	0.74	0.45	0.93	0.99	0.99	0.99

492

493 **Table A2: Comparison of precipitation intensity based on weighing rain gauge and 2DVD observation data for each  $T_w$  range.**

		T1	T2	T3	T4	T5	T6	T7	T8	T9	T10
Unfiltered	$a_I$	7.36	3.39	3.98	3.86	2.25	2.15	1.37	1.01	1.03	1.03
	$a_0$	0.09	0.12	0.27	0.09	0.24	0.06	0.04	0.04	0.02	0.01
	RMSE	1.04	0.88	0.95	0.93	0.76	0.64	0.33	0.14	0.12	0.17
	MAE	0.44	0.46	0.57	0.43	0.43	0.31	0.15	0.08	0.07	0.12
	MAPE	49.76	55.42	60.80	48.81	53.44	41.61	41.39	22.03	13.07	19.05
	CC	0.98	0.97	0.90	0.93	0.88	0.89	0.95	0.98	0.99	0.99
Method 1	$a_I$	0.61	0.26	0.48	0.93	0.48	0.61	1.11	0.97	0.98	0.98
	$a_0$	0.02	0.03	0.06	0.05	0.09	0.05	0.04	0.05	0.02	0.01
	RMSE	0.13	0.17	0.13	0.19	0.28	0.20	0.20	0.13	0.10	0.14
	MAE	0.06	0.07	0.07	0.12	0.13	0.11	0.10	0.08	0.07	0.10
	MAPE	25.71	63.33	41.35	41.49	36.12	79.17	38.21	22.17	14.21	21.89
	CC	0.70	0.65	0.73	0.80	0.79	0.71	0.96	0.98	0.99	1.00

Method 2	$a_I$	0.53	0.58	0.21	0.46	0.28	0.80	0.88	0.95	0.94	0.93
	$a_0$	0.01	0.00	0.01	0.03	0.06	0.01	0.05	0.03	0.03	0.02
	RMSE	0.07	0.03	0.09	0.18	0.31	0.10	0.11	0.12	0.11	0.17
	MAE	0.02	0.01	0.06	0.11	0.15	0.07	0.07	0.07	0.07	0.12
	MAPE	22.22	11.11	28.57	85.56	55.43	27.34	35.56	18.32	14.12	20.69
	CC	0.82	0.94	0.45	0.75	0.78	0.92	0.98	0.98	1.00	1.00
Method 3	$a_I$	1.91	2.01	2.33	2.02	0.92	1.04	1.12	1.01	1.03	1.03
	$a_0$	0.07	0.10	0.15	0.10	0.15	0.10	0.05	0.04	0.02	0.01
	RMSE	0.22	0.41	0.52	0.45	0.29	0.21	0.16	0.14	0.12	0.17
	MAE	0.12	0.25	0.29	0.24	0.16	0.13	0.09	0.08	0.07	0.12
	MAPE	42.13	49.58	52.32	44.83	46.50	37.92	34.21	22.03	13.07	19.05
	CC	0.91	0.98	0.86	0.90	0.80	0.90	0.98	0.98	0.99	0.99
Method 1 (melted)	$a_I$	1.16	0.65	0.89	1.12	0.57	0.79	1.15	0.99	0.99	0.98
	$a_0$	0.05	0.03	0.09	0.06	0.12	0.06	0.04	0.04	0.02	0.01
	RMSE	0.11	0.13	0.16	0.23	0.26	0.16	0.21	0.13	0.10	0.13
	MAE	0.06	0.08	0.10	0.11	0.15	0.10	0.09	0.08	0.06	0.10
	MAPE	30.25	31.05	36.50	29.44	49.92	32.10	37.80	22.22	13.91	21.50
	CC	0.90	0.97	0.82	0.82	0.77	0.89	0.96	0.98	1.00	1.00
Method 2 (melted)	$a_I$	0.91	0.53	0.65	0.74	0.38	0.61	0.93	0.96	0.95	0.95
	$a_0$	0.01	0.02	0.07	0.05	0.09	0.04	0.05	0.04	0.02	0.01
	RMSE	0.04	0.18	0.14	0.17	0.29	0.18	0.09	0.12	0.11	0.15
	MAE	0.01	0.10	0.09	0.11	0.14	0.10	0.06	0.07	0.07	0.11
	MAPE	8.89	35.56	34.62	42.75	58.79	40.35	34.42	17.78	14.24	22.16
	CC	0.98	0.98	0.79	0.82	0.77	0.87	0.99	0.98	1.00	1.00
Method 3 (melted)	$a_I$	2.24	2.10	2.47	2.08	0.99	1.14	1.13	1.01	1.03	1.03
	$a_0$	0.07	0.10	0.16	0.11	0.16	0.10	0.05	0.04	0.02	0.01
	RMSE	0.27	0.44	0.55	0.48	0.30	0.22	0.16	0.14	0.12	0.17
	MAE	0.14	0.26	0.32	0.25	0.17	0.14	0.09	0.08	0.07	0.12
	MAPE	43.48	49.81	51.47	45.14	46.83	38.15	37.14	22.03	13.07	19.05
	CC	0.93	0.98	0.86	0.89	0.82	0.92	0.98	0.98	0.99	0.99

494 Table A3: Diameter channel information of the PARSIVEL disdrometer.

Channel number	Mid-value of channel (mm)	Diameter spread (mm)	Channel number	Mid-value of channel (mm)	Diameter spread (mm)
1	0.062	0.125	17	3.250	0.500

2	0.187	0.125	18	3.750	0.500
3	0.312	0.125	19	4.250	0.500
4	0.437	0.125	20	4.750	0.500
5	0.562	0.125	21	5.500	1.000
6	0.687	0.125	22	6.500	1.000
7	0.812	0.125	23	7.500	1.000
8	0.937	0.125	24	8.500	1.000
9	1.062	0.125	25	9.500	1.000
10	1.187	0.125	26	11.000	2.000
11	1.375	0.250	27	13.000	2.000
12	1.625	0.250	28	15.000	2.000
13	1.875	0.250	29	17.000	2.000
14	2.125	0.250	30	19.000	2.000
15	2.375	0.250	31	21.500	3.000
16	2.750	0.500	32	24.500	3.000

495 **Table A4: Velocity channel information of the PARSIVEL disdrometer.**

Channel number	Mid-value of channel (mm)	Velocity spread (mm)	Channel number	Mid-value of channel (mm)	Velocity spread (mm)
1	0.050	0.100	17	2.600	0.400
2	0.150	0.100	18	3.000	0.400
3	0.250	0.100	19	3.400	0.400
4	0.350	0.100	20	3.800	0.400
5	0.450	0.100	21	4.400	0.800
6	0.550	0.100	22	5.200	0.800
7	0.650	0.100	23	6.000	0.800
8	0.750	0.100	24	6.800	0.800
9	0.850	0.100	25	7.600	0.800
10	0.950	0.100	26	8.800	1.600
11	1.100	0.200	27	10.400	1.600
12	1.300	0.200	28	12.000	1.600
13	1.500	0.200	29	13.600	1.600
14	1.700	0.200	30	15.200	1.600

15	1.900	0.200	31	17.600	3.200
16	2.200	0.400	32	20.800	3.200

496 **Author contributions**

497 HJK and CJ, conceptualized the project. JB did the data curation and formal analysis. HJK and SHS did the analysis and  
498 interpretation. HJK and JB led the investigation. HJK prepared the original draft, and SHS and CJ reviewed and edited the  
499 paper. All authors have read and agreed to the published version of the paper.

500 **Acknowledgements**

501 This study was supported by the Basic Science Research Program through the National Research Foundation of Korea  
502 (NRF), funded by the Ministry of Education (RS-2022-NR071182).

503

504 **Competing Interest**

505 The contact author has declared that none of the authors has any competing interests.

506 **References**

- 507 Atlas, D., Srivastava, R. C., and Sekhon, R. S.: Doppler radar characteristics of precipitation at vertical incidence, *Rev.*  
508 *Geophys.*, 11, 1–35. <https://doi.org/10.1029/RG011i001p00001>, 1973.
- 509 Barthazy, E. and Schefold, R.: Fall velocity of snowflakes of different riming degree and crystal types, *Atmos. Res.*, 82,  
510 391–398. <https://doi.org/10.1016/j.atmosres.2005.12.009>, 2006.
- 511 Beard, K. V.: Terminal velocity adjustment for cloud and precipitation drops aloft, *J. Atmos. Sci.*, 34, 1293–1298.  
512 [https://doi.org/10.1175/1520-0469\(1977\)034<1293:TVAFCA>2.0.CO;2](https://doi.org/10.1175/1520-0469(1977)034<1293:TVAFCA>2.0.CO;2), 1977.
- 513 Brandes, E. A., Zhang, G., and Vivekanandan, J.: Experiments in rainfall estimation with a polarimetric radar in a  
514 subtropical environment, *J. Appl. Meteor.*, 41, 674–685. [https://doi.org/10.1175/1520-0450\(2002\)041<0674:EIREWA>2.0.CO;2](https://doi.org/10.1175/1520-0450(2002)041<0674:EIREWA>2.0.CO;2), 2002.
- 516 Chang, W. Y., Wang, T. C. C., and Lin, P. L.: Characteristics of the raindrop size distribution and drop shape relation in  
517 typhoon systems in the western Pacific from the 2D video disdrometer and NCU C-band polarimetric radar, *J. Atmos.*  
518 *Ocean. Technol.*, 26, 1973–1993. <https://doi.org/10.1175/2009JTECHA1236.1>, 2009.
- 519 Dahlström, B.: Cloud physical and climatological factors for the determination of rain intensity, *Water*, 13, 2292.  
520 <https://doi.org/10.3390/w13162292>, 2021.
- 521 Delanoë, J., Protat, A., Testud, J., Bouniol, D., Heymsfield, A. J., Bansemer, A., Brown, P. R. A., Forbes, R. M.: Statistical  
522 properties of the normalized ice particle size distribution, *J. Geophys. Res. Atmos.*, 110.  
523 <https://doi.org/10.1029/2004JD005405>, 2005.

524 Deo, A. and Walsh, K. J. E.: Contrasting tropical cyclone and non-tropical cyclone related rainfall drop size distribution at  
525 Darwin, Australia, *Atmos. Res.*, 181, 81–94. <https://doi.org/10.1016/j.atmosres.2016.06.015>, 2016.

526 Ding, B., Yang, K., Qin, J., Wang, L., Chen, Y., and He, X.: The dependence of precipitation types on surface elevation and  
527 meteorological conditions and its parameterization, *J. Hydrol.*, 513, 154–163.  
528 <https://doi.org/10.1016/j.jhydrol.2014.03.038>, 2014.

529 Du, Y. and Chen, G.: Heavy rainfall associated with double low-level jets over southern China. Part II: Convection initiation,  
530 *Mon. Weather Rev.*, 147, 543–565. <https://doi.org/10.1175/MWR-D-18-0102.1>, 2019.

531 Friedrich, K., Kalina, E. A., Masters, F. J., and Lopez, C. R.: Drop-size distributions in thunderstorms measured by optical  
532 disdrometers during VORTEX2, *Mon. Weather Rev.*, 141, 1182–1203. <https://doi.org/10.1175/MWR-D-12-00116.1>,  
533 2013.

534 Gong, Y., He, T., Chen, M., Wang, B., Nie, L., and Yin, Y.: Spatio-temporal enhanced contrastive and contextual learning  
535 for weather forecasting, *IEEE Trans. Knowl. Data Eng.*, 36, 4260–4274. <https://doi.org/10.1109/TKDE.2024.3362825>,  
536 2024.

537 Grazioli, J., Tuia, D., Monhart, S., Schneebeli, M., Raupach, T., and Berne, A.: Hydrometeor classification from two-  
538 dimensional video disdrometer data, *Atmos. Meas. Tech.*, 7, 2869–2882. <https://doi.org/10.5194/amt-7-2869-2014>,  
539 2014.

540 Guo, J., Liu, H., Li, Z., Rosenfeld, D., Jiang, M., Xu, W., Jiang, J. H., He, J., Chen, D., Min, M., Zhai, P.: Aerosol-induced  
541 changes in the vertical structure of precipitation: A perspective of TRMM precipitation radar, *Atmos. Chem. Phys.*, 18,  
542 13329–13343. <https://doi.org/10.5194/acp-18-13329-2018>, 2018.

543 Hu, A. Z. and Igel, A. L.: A bin and a bulk microphysics scheme can be more alike than two bin schemes, *J. Adv. Model.*  
544 *Earth Syst.*, 15, MS003303, e2022. <https://doi.org/10.1029/2022MS003303>, 2023.

545 Insel, N., Poulsen, C. J., and Ehlers, T. A.: Influence of the Andes Mountains on South American moisture transport,  
546 convection, and precipitation, *Clim. Dyn.*, 35, 1477–1492. <https://doi.org/10.1007/s00382-009-0637-1>, 2010.

547 Iversen, E. C., Thompson, G., and Nygaard, B. E.: Improvements to melting snow behavior in a bulk microphysics scheme,  
548 *Atmos. Res.*, 253, 105471. <https://doi.org/10.1016/j.atmosres.2021.105471>, 2021.

549 Jaffrain, J. and Berne, A.: Experimental quantification of the sampling uncertainty associated with measurements from  
550 PARSIVEL disdrometers, *J. Hydrol. Meteorol.*, 12, 352–370. <https://doi.org/10.1175/2010JHM1244.1>, 2011.

551 Ji, L., Chen, H., Li, L., Chen, B., Xiao, X., Chen, M., and Zhang, G.: Raindrop size distributions and rain characteristics  
552 observed by a PARSIVEL disdrometer in Beijing, Northern China, *Remote Sens.*, 11, 1479.  
553 <https://doi.org/10.3390/rs11121479>, 2019.

554 Kim, H. J., Jung, W., Suh, S. H., Lee, D. I., and You, C. H.: The characteristics of raindrop size distribution at windward and  
555 leeward side over mountain area, *Remote Sens.*, 14, 2419. <https://doi.org/10.3390/rs14102419>, 2022.

556 Kim, H. J., Lee, K. O., You, C. H., Uyeda, H., and Lee, D. I.: Microphysical characteristics of a convective precipitation  
557 system observed on July 04, 2012, over Mt. Halla in South Korea, *Atmos. Res.*, 222, 74–87.  
558 <https://doi.org/10.1016/j.atmosres.2019.02.011>, 2019.

559 Kochendorfer, J., Earle, M. E., Hodyss, D., Reverdin, A., Roulet, Y. A., Nitu, R., Rasmussen, R., Landolt, S., Buisán, S.,  
560 Laine, T.: Undercatch adjustments for tipping-bucket gauge measurements of solid precipitation, *J. Hydrol. Meteorol.*,  
561 21, 1193–1205. <https://doi.org/10.1175/JHM-D-19-0256.1>, 2020.

562 Kruger, A. and Krajewski, W. F.: Two-dimensional video disdrometer: A description, *J. Atmos. Ocean. Technol.*, 19, 602–  
563 617. [https://doi.org/10.1175/1520-0426\(2002\)019<0602:TDYDAD>2.0.CO;2](https://doi.org/10.1175/1520-0426(2002)019<0602:TDYDAD>2.0.CO;2), 2002.

564 Lee, K. O., Uyeda, H., and Lee, D. I.: Microphysical structures associated with enhancement of convective cells over Mt.  
565 Halla, Jeju Island, Korea on 6 July 2007, *Atmos. Res.*, 135–136, 76–90.  
566 <https://doi.org/10.1016/j.atmosres.2013.08.012>, 2014.

567 Lintner, B. R., Adams, D. K., Schiro, K. A., Stansfield, A. M., Amorim Rocha, A. A., and Neelin, J. D.: Relationships  
568 among climatological vertical moisture structure, column water vapor, and precipitation over the central Amazon in  
569 observations and CMIP5 models, *Geophys. Res. Lett.*, 44, 1981–1989. <https://doi.org/10.1002/2016GL071923>, 2017.

570 Liu, X., Li, H., Hu, S., Wan, Q., Xiao, H., Zheng, T., Li, M., Ye, L., Guo, Z., Wang, Y., Yan, Z.: A high-precision and fast  
571 solution method of gamma raindrop size distribution based on 0-moment and 3-moment in South China, *J. Appl.*  
572 *Meteorol. Climatol.*, 60, 1407–1421. <https://doi.org/10.1175/JAMC-D-21-0043.1>, 2021.

573 Lu, Y., Yu, Z., Albertson, J. D., Chen, H., Hu, L., Pendergrass, A., Chen, X., Li, Q.: Understanding the influence of urban  
574 form on the spatial pattern of precipitation, *Earths Future*, 12, EF003846, e2023.  
575 <https://doi.org/10.1029/2023EF003846>, 2024.

576 Maheskumar, R. S., Padmakumari, B., Konwar, M., Morwal, S. B., and Deshpande, C. G.: Characterization of hydrometeors  
577 and precipitation over the Indian monsoon region using aircraft measurements, *Atmos. Res.*, 205, 147–154.  
578 <https://doi.org/10.1016/j.atmosres.2018.02.012>, 2018.

579 Marshall, J. S. and Palmer, W. M. K.: The distribution of raindrops with size, *J. Atmos. Sci.*, 5, 165–166.  
580 [https://doi.org/10.1175/1520-0469\(1948\)005<0165:TDORWS.2.0.CO;2](https://doi.org/10.1175/1520-0469(1948)005<0165:TDORWS.2.0.CO;2), 1948.

581 Marzuki, M., Randeu, W. L., Schönhuber, M., Bringi, V. N., Kozu, T., and Shimomai, T.: Raindrop size distribution  
582 parameters of distrometer data with different bin sizes, *IEEE Trans. Geosci. Remote Sens.*, 48, 3075–3080.  
583 <https://doi.org/10.1109/TGRS.2010.2043955>, 2010.

584 [Ong, C. R., Miura, H., Koike, M.: The terminal velocity of axisymmetric cloud drops and raindrops evaluated by the](#)  
585 [immersed boundary method. \*J. Atmos Sci.\*, 78\(4\), 1129–1146. <https://doi.org/10.1175/JAS-D-20-0161.1>, 2021.](#)

586 Padullés, R., Kuo, Y. H., Neelin, J. D., Turk, F. J., Ao, C. O., and De la Torre Juárez, M.: Global tropical precipitation  
587 relationships to free-tropospheric water vapor using radio occultations, *J. Atmos. Sci.*, 79, 1585–1600.  
588 <https://doi.org/10.1175/JAS-D-21-0052.1>, 2022.

서식 지정함: 글꼴 색 텍스트1

서식 지정함: 글꼴 색 빨강

589 Raupach, T. H. and Berne, A.: Correction of raindrop size distributions measured by Parsivel disdrometers, using a two-  
590 dimensional video disdrometer as a reference, *Atmos. Meas. Tech.*, 8, 343–365. [https://doi.org/10.5194/amt-8-343-](https://doi.org/10.5194/amt-8-343-2015)  
591 [2015](https://doi.org/10.5194/amt-8-343-2015), 2015.

592 Savina, M., Schäppi, B., Molnar, P., Burlando, P., and Sevruk, B.: Comparison of a tipping-bucket and electronic weighing  
593 precipitation gage for snowfall, *Atmos. Res.*, 103, 45–51. <https://doi.org/10.1016/j.atmosres.2011.06.010>, 2012.

594 Segovia-Cardozo, D. A., Rodríguez-Sinobas, L., Díez-Herrero, A., Zubeizu, S., and Canales-Ide, F.: Understanding the  
595 mechanical biases of tipping-bucket rain gauges: A semi-analytical calibration approach, *Water*, 13, 2285.  
596 <https://doi.org/10.3390/w13162285>, 2021.

597 Serio, M. A., Carollo, F. G., and Ferro, V.: Raindrop size distribution and terminal velocity for rainfall erosivity studies. A  
598 review, *J. Hydrol.*, 576, 210–228. <https://doi.org/10.1016/j.jhydrol.2019.06.040>, 2019.

599 Smith, P. L.: Raindrop size distributions: Exponential or gamma—Does the difference matter?, *J. Appl. Meteor.*, 42, 1031–  
600 1034. [https://doi.org/10.1175/1520-0450\(2003\)042<1031:RSDEOG>2.0.CO;2](https://doi.org/10.1175/1520-0450(2003)042<1031:RSDEOG>2.0.CO;2), 2003.

601 Steenburgh, W. J.: Sea-effect precipitation: A Look at Japan’s “Gosetsu Chitai”, *Bull. Am. Meteorol. Soc.*, 101, 129–136.  
602 <https://doi.org/10.1175/BAMS-D-18-0335.A>, 2020.

603 Stull, R.: Wet-bulb temperature from relative humidity and air temperature, *J. Appl. Meteorol. Climatol.*, 50, 2267–2269.  
604 <https://doi.org/10.1175/JAMC-D-11-0143.1>, 2011.

605 Sypka, P.: Dynamic real-time volumetric correction for tipping-bucket rain gauges, *Agric. Forest Meteorol.*, 271, 158–167.  
606 <https://doi.org/10.1016/j.agrformet.2019.02.044>, 2019.

607 Tang, Y. S., Chang, P. L., Chang, W. Y., Zhang, J., Tang, L., Lin, P. F., and Chen, C. R.: A localized quantitative  
608 precipitation estimation for S-band polarimetric radar in Taiwan, *J. Hydrol. Meteorol.*, 25, 1697–1712.  
609 <https://doi.org/10.1175/JHM-D-23-0205.1>, 2024.

610 Thomas, A., Kanawade, V. P., Chakravarty, K., and Srivastava, A. K.: Characterization of raindrop size distributions and its  
611 response to cloud microphysical properties, *Atmos. Res.*, 249, 105292.  
612 <https://doi.org/10.1016/j.atmosres.2020.105292>, 2021.

613 Thurai, M. and Bringi, V. N.: Drop axis ratios from a 2D video disdrometer, *J. Atmos. Ocean. Technol.*, 22, 966–978.  
614 <https://doi.org/10.1175/JTECH1767.1>, 2005.

615 Tiira, J., Moisseev, D. N., Von Lerber, A., Ori, D., Tokay, A., Bliven, L. F., and Petersen, W.: Ensemble mean density and  
616 its connection to other microphysical properties of falling snow as observed in Southern Finland, *Atmos. Meas. Tech.*,  
617 9, 4825–4841. <https://doi.org/10.5194/amt-9-4825-2016>, 2016.

618 Ulbrich, C. W.: Natural variations in the analytical form of the raindrop size distribution, *J. Clim. Appl. Meteorol.*, 22, 1764–  
619 1775. [https://doi.org/10.1175/1520-0450\(1983\)022<1764:NVITAF>2.0.CO;2](https://doi.org/10.1175/1520-0450(1983)022<1764:NVITAF>2.0.CO;2), 1983.

620 Vázquez-Martín, S., Kuhn, T., and Eliasson, S.: Mass of different snow crystal shapes derived from fall speed measurements,  
621 *Atmos. Chem. Phys.*, 21, 18669–18688. <https://doi.org/10.5194/acp-21-18669-2021>, 2021.

622 [Wang, P. K. and Pruppacher, H. R.: Acceleration to terminal velocity of cloud and raindrops. \*J. Appl. Meteorol. Clim.\*, 16\(3\),](#)  
623 [275–280. \[https://doi.org/10.1175/1520-0450\\(1977\\)016<0275:ATTVOC>2.0.CO;2\]\(https://doi.org/10.1175/1520-0450\(1977\)016<0275:ATTVOC>2.0.CO;2\), 1977.](#)

624 Wen, L., Zhao, K., Chen, G., Wang, M., Zhou, B., Huang, H., Hu, D., Lee, W. C., Hu, H.: Drop size distribution  
625 characteristics of seven typhoons in China, *J. Geophys. Res. Atmos.*, 123, 6529–6548.  
626 <https://doi.org/10.1029/2017JD027950>, 2018.

627 Yang, Q., Dai, Q., Han, D., Chen, Y., and Zhang, S.: Sensitivity analysis of raindrop size distribution parameterizations in  
628 WRF rainfall simulation, *Atmos. Res.*, 228, 1–13. <https://doi.org/10.1016/j.atmosres.2019.05.019>, 2019.

629 Yang, Y., Wang, R., Chen, F., Liu, C., Bi, X., and Huang, M.: Synoptic weather patterns modulate the frequency, type and  
630 vertical structure of summer precipitation over Eastern China: A perspective from GPM observations, *Atmos. Res.*, 249,  
631 105342. <https://doi.org/10.1016/j.atmosres.2020.105342>, 2021.

632 Yao, X., Yang, K., Zhou, X., Wang, Y., Lazhu, C., Chen, Y., and Lu, H.: Surface friction contrast between water body and  
633 land enhances precipitation downwind of a large lake in Tibet, *Clim. Dyn.*, 56, 2113–2126.  
634 <https://doi.org/10.1007/s00382-020-05575-x>, 2021.

635 Yi, Y., Yi, F., Liu, F., Zhang, Y., Yu, C., and He, Y.: Microphysical process of precipitating hydrometeors from warm-front  
636 mid-level stratiform clouds revealed by ground-based lidar observations, *Atmos. Chem. Phys.*, 21, 17649–17664.  
637 <https://doi.org/10.5194/acp-21-17649-2021>, 2021.  
638

저식 지정함: 글꼴 색 텍스트1

저식 지정함: 글꼴 색 텍스트1

저식 지정함: 하이퍼링크, 글꼴 굵게, 글꼴 색 자동